INVESTIGATION OF AC MAGNETIC PROPERTIES OF MAGNETITE OBTAINED FROM COX'S BAZAR BEACH SAND

A Dissertation Submitted to the Department of Physics, Bangladesh University of Engineering & Technology, Dhaka, in Partial Fulfillment of the Requirement for the Degree of Master of Philosophy in Physics

SUBMITTED BY

Md. Jahangir Alam

EXAMINATION ROLL NO. : **040414009F**
REGISTRATION NO. : **0404537**
SESSION : **April - 2004**

DEPARTMENT OF PHYSICS
BANGLADESH UNIVERSITY OF ENGINEERING & TECHNOLOGY
DHAKA 1000, BANGLADESH

CANDIDATE'S DECLARATION

It is hereby declared that this thesis or any part of it has not been submitted elsewhere for the award of any degree or diploma.

MD. JAHANGIR ALAM

BANGLADESH UNIVERSITY OF ENGINEERING & TECHNOLOGY
DEPARTMENT OF PHYSICS, DHAKA 1000, BANGLADESH

CERTIFICATION OF THESIS

The thesis titled "**INVESTIGATION OF AC MAGNETIC PROPERTIES OF MAGNETITE OBTAINED FROM COX'S BAZAR BEACH SAND**" submitted by **Md. Jahangir Alam**, Roll No.: 040414009F, Session: April 2004, has been accepted as satisfactory in partial fulfillment of the requirement for the degree of **Master of Philosophy** in Physics on December 27, 2009.

BOARD OF EXAMINERS

1. (A. Hossain.) Chairman
Dr. A. K. M. Akther Hossain (Supervisor)
Professor, Department of Physics, BUET.

2. (A. Hossain.) Member (Ex-Officio)
Head, Department of Physics
BUET.

3. (F. Khanam.) Member
Mrs. Fahima Khanam,
Associate Professor
Department of Physics, BUET.

4. ( ) Member (External)
Dr. Khandker Saadat Hossain
Assistant Professor
Department of Physics,
University of Dhaka

DEDICATED TO

MY
BELOVED
PARENTS

ACKNOWLEDGEMENTS

I firstly express all of my admiration and devotion to the almighty Allah, the most beneficial who has enabled me to perform this research work and to submit this thesis.

I express my profound gratitude to my honourable supervisor Prof. A.K.M. Akther Hossain, Department of Physics, BUET, for his constant direction, constructive criticism and inspiration in pursuing the whole investigation of the present research. Words are always insufficient to express his working capacities and unending enthusiasm for scientific rigorousness for innovative investigations. This always becomes the everlasting source of inspiration for his students.

I am deeply grateful to Head, Department of Physics, BUET, for his kind permission to do this work. I am also grateful to BUET authority for providing the financial grant for this research.

I would like to express my gratitude to Professor Mominul Huq, Professor Md. Abu Hashan Bhuiyan, Professor Nazma Zaman, Professor Jiban Podder, Mrs. Fahima Khanam, Dr. Nazrul Islam, Dr. Afia Begum, Dr Md. Rafi Uddin, Dr. Md. Forhad Mina, Mr. M. Sameer Ullah, Mr. M. A.S. Karal, Mr. Md Jellur Rahman,Mr.Muhammad Ruhul Amin and all other teachers of Physics Department (BUET), and Md.Abdul Hamidur Rahman Khan, Lecturer,Ahsanullah University of Science & Technology for their cooperation.

I wish to thank specially Professor Md. Helal Uddin ,Principal, and all teachers of Chillahati Govt. College and Shahabuddin sir, Poritoskumar Mondal, for their inspiration and also my senior research worker Shaikh Tawhid Mahmud, Md. Khairul Kabir, Omar Faruk, Farhad vi, Kharshed vi ,Mahabub vi for their cooperation throughout the study. I am also grateful to my friends Reaj, yeakub, Ridoy for their inspiration and encouragement. I also gratefully acknowledge the wishes of my younger researchers Binundita, Maruf, Abdur Rahman for their constant support.

Ultimately, I would mention a very special gratefulness for the moral support and sustaining inspiration provided by the members of my family. This dissertation would never have been possible without their love and affection.

The Author

Md. Jahangir Alam

ABSTRACT

In Bangladesh, Cox's Bazar beach sand contains potentially valuable minerals as discovered during a geological survey for radioactive minerals in 1961. Beach sand contains magnetic materials in the form of magnetite. Beach sand was collected from Kolatoli sea beach; Cox's Bazar, was washed by water to separate other unnecessary materials such as small rock, clay, etc. Afterward, the sand was dried and finally separated by strong magnet. Obtained magnetite powders were ground by ball milling for several hours in water media. The coarse particle fractions were eliminated by sedimentation. The raw powders are then sintered at 750°C and 900°C for 1 h. X-ray diffraction studies show that the raw powders sintered at 750°C is the best samples. From this dried fine powder of magnetite toroid and disk-shaped samples were prepared by uniaxial pressing and sintered at various temperatures for varions dwell times. Structural, DC and AC magnetization, and electrical transport properties of these sintered magnetites were investigated thoroughly. X-ray diffraction studies show that the magnetite forms spinel structure with some impurities. It was observed that the magnetite separated from beach sand shows Verwey transition at 125 K. The sintered magnetite has highest magnetization about 3.5 μ_B which is about 88% magnetization value of the pure magnetite. Real part of the initial permeability, μ_i', also varies with sintering temperature and sintering time. For a fixed sintering temperature, it is observed that μ_i' values increases as the sintering time increase, perhaps due to improved microstructure.

Utilizing magnetite from the beach sand and commercially available ZnO, the $Fe_{3-x}Zn_xO_4$ (x = 0.30 and 0.5) ferrites were prepared by a conventional solid state reaction technique. The samples were sintered at 750°C in air for 1 h. Structural investigation of these ferrites was studied by x-ray diffraction. It was observed that the lattice parameter increases as the Zn content increases, which obey the Vegards law. The DC and AC magnetic properties are also investigated using SQUID magnetometer and Impedance Analyzer, respectively. It was observed that the magnetization values fall drastically due to the substitution of Zn. This result can be explained with the help of cation distribution in the A-site and B-site in the spinel structure. However, the real part of the permeability increases and loss factor decreases due to Zn substitution in magnetite.

CONTENTS

CHAPTER 1

CHAPTER 2

CHAPTER 3

CHAPTER 4

RESULTS AND DISCUSSION 45-70

CHAPTER 5

LIST OF FIGURES

Pages

LIST OF TABLES

LIST OF SYMBOLS AND ABBREVIATIONS

AC	Alternating current
B	Magnetic induction
CMR	Colossal magnetoresistance
$F(\theta)$	Nelson-Riley function
f_r	Resonance frequency
g	Landé splitting factor
H_{cr}	Critical field
J	Exchange integral
K	Total anisotropy
K_1	Magnetocrystalline anisotropy constant
L_s	Self-inductance of the sample core
L_o	Inductance of the winding coil without sample
M	Magnetization
M_s	Saturation magnetization
N_A	Avogadro's number
P_{intra}	Intragranular porosity
P_{inter}	Intergranular porosity
P_e	Eddy-current loss
Q	Relative quality factor
T_c	Curie temperature
T_n	Néel temperature
T_s	Sintering temperature
$tan\delta$	Loss factor
Z	Complex impedance
α	Restoring force coefficient
β	Viscous damping factor
γ	Domain wall energy
ω	Angular velocity
δ_w	Domain wall thickness
μ_i	Initial permeability
μ'	Real part of complex permeability
μ''	Imaginary part of complex permeability
μ_B	Bohr magneton
χ_{spin}	Intrinsic rotational susceptibility
χ_w	Domain wall susceptibility

CHAPTER 1

INTRODUCTION

1.1 Introduction

Ferrites are ceramic materials formed by reacting metal oxides into magnetic materials. Research activity on ferrites intense in the last 50 years as a consequence of Sonek's work [1]. Ferrites are becoming increasingly important as high frequency core materials because they combine useful ferromagnetic properties with electrical resistivity [2-4]. Practically, all ferrite materials have the same crystal structure as the mineral spinel may be regarded as a cubic [5]. According to their structure spinel-type ferrites are natural superlattices. It has tetrahedral *A*-site and octahedral *B*-site in AB_2O_4 crystal structure. It shows various magnetic properties depending on the composition and cation distribution. Various cations can be placed in *A*-site and *B*-site to tune its magnetic properties. Depending on *A*-site and *B*-site cations it can exhibit ferrimagnetic, antiferromagnetic, spin (cluster) glass, and paramagnetic behavior [6]. Due to their fascinating behavior of magnetic and electric properties they are subjects of intense theoretical and experimental investigation for various applications [7]. These polycrystalline spinel ferrites are widely used in many electronic devices. They are preferred because of their high permeability in the radio – frequency (RF) region, high electrical resistivity, mechanical hardness and chemical stability [8]. Ferrites are also useful to prevent and eliminate RF Interference to audio devices [9,10].

In Bangladesh, Cox's Bazar beach sand contains potentially valuable minerals as discovered during a geological survey for radioactive minerals in 1961. Beach sand contains magnetic materials in the form of magnetite (Fe_3O_4). So far there is no report regarding the systematic investigation of magnetite obtain from beach sand. In the present studies ac magnetic properties of the magnetite will be investigated. Magnetic properties of some mixed spinel-type $Fe_{3-x}Zn_xO_4$ ferrite using magnetite from beach sand will also be investigated.

1.2 Objectives with specific aims and possible outcome

Ferrites are especially convenient for high frequency uses because of their high resistivity. The high frequency response of the complex permeability is therefore very useful in determining the convenient frequency range in which a particular ferrite material can be used. The mechanism of eddy current losses and damping of domain wall motion can be understood from the relative magnitudes of the real and imaginary parts of the complex permeability. The effect of composition and microstructure on the frequency response is therefore very useful.

The main objectives of the present research are as follows:

- Separation of magnetite from beach sand.
- Preparation of magnetite samples and Zn substituted magnetite ($Fe_{3-x}Zn_xO_4$ for x=0.3 and 0.5)
- Density of the samples
- DC magnetization of the magnetite separated from the beach sand.
- Complex initial permeability as a function of frequency (1 KHz-13MHz) for samples sintered at various temperatures and various times.

Possible outcome of the research is as follows:

- Magnetization and initial complex permeability studies will reveal the properties of magnetite separated from the beach sand. The obtained magnetization and permeability are helpful for the device fabrication. Our country is very much dependent on the imported ferrite cores and others soft magnetic materials. If the separated magnetite from the beach sand has desired characteristics, importation can be stopped that will save foreign currency.
- Results obtained from the present research are important from physics point of view and also will be helpful for practical applications of the above mentioned magnetite and other mixed ferrites.

1.3 Outeline of the Thesis

The format of the thesis is as follows:

Chapter 1 of this thesis deals with the introduction and importance of ferrites and objectives of the present work.

Chapter 2 gives a brief overview of the materials, theoretical background as well as crystal structure of the spinel type ferrites.

Chapter 3 gives the details of the sample preparation and describes the descriptions of different measurements that have been used in this research work.

Chapter 4 is devoted to the results of various investigations of the study and explanation of results in the light of existing theories.

The conclusions drawn from the overall experimental results and discussion are presented in Chapter 5.

References:

[1] Snoek, J. L. "Dispersion and absorptions in magnetic ferrites at frequencies above Mc/s," *Physica*, Vol-14, pp207-217, (1948).

[2] Mahmud, S. T., Hossain, A. K. M. A., Hakim, A.K.M.A., Seki, M., Kawai,T., and Tabata, H., "Influence of microstructure on the complex permeability of spinel type Ni-Zn ferrite," *Journal of Magnetism and Magnetic Materials*,Vol- **305**, pp269-274, (2006).

[3] Hossain, A. K. M. A., Seki, M., Kawai,T., and Tabata, H., "Colossal magnetoresistance in spinel type $Zn_{1-x}Ni_xFe_2O_4$," *Journal of Applid Physics, Vol-* **96**, No. 2, pp1237-1275, (2004).

[4] Sattar, A. A., H. M. El-Sayed, K. M. El-Shokrofy and El-Tabey, M. M., "Improvement of the magnetic properties of Mn-Ni-Zn ferrite by the non-magnetic Al^{3+} ion substitution," *Journal of Applied Science.*, Vol- **5**, No. 1, pp162-168, (2005).

[5] Bragg, W. H., "The structure of the spinel group of crystals". *Philosophical Magagine*, Vol-**30**, pp 305-315, (1915)

[6] Rezlescu, E., Sachelarie, L., Popa, P. D. and Rezlescu, N., "Effect of substitution of diavalent ions on the electrical and magnetic properties of Ni-Zn-Me ferrites," *IEEE Transactions on Magnetics*, Vol-**36**, No. 6, pp3962-3967, (2000).

[7] Caltun, O. F., Spinu, L. and Stancu, A., "Magnetic properties of high frequency Ni-Zn ferrites doped with Cuo". *IEEE Transactions on Magnetics, Vol-37, No. 4, pp23-53, (2001).*

[8] Goldman, A., "Handbook of Modern Ferromagnetic Materials," Kulwer Acad. Pub, Boston, U.S.A., pp165, (1999).

[9] Caltun, O. F., Spinu, L., and Stancu. A., "Structure and magnetic properties of Ni-Zn-Cu ferrites sintered at different temperatures" *Journal of Optoelectronics and Advanced Materials*,Vol- **4**, No. 2, pp 337-340, (2002).

[10] Morrison, S. A., Cahill, C. L., Swaminathan, Raja, McHenry, M. E., and Harris,V. G., "Magnetic and structural properties of nickel-zinc ferrite nano-particles synthesized at room temperature," *Journal of Applid Physics, Vol-* **95**, No. 11, pp6392-6395, (2004).

CHAPTER 2

LITERATURE REVIEW

Double oxides of iron and other metals are important members of ferrimagnetic system commonly known as ferrites. The outstanding properties of ferrites are their complex magnetic structure, which can be varied to tailor their magnetic properties for various high frequency applications. In this chapter we describe a brief overview of the ferrites. The basic issue of ferrimagnetism, crystal structure of the spinel ferrites and effect of non-magnetic Zn substitution on the magnetic moments in spinel ferrites are discussed. A few theoretical aspects of complex permeability are also discussed.

2.1 Overview of the Materials

Ferrites commonly expressed by the general chemical formula $MeO.Fe_2O_3$, where *Me* represents divalent metals, first commanded the public attention when Hilpert (1909) focused on the usefulness of ferrites at high frequency [1]. A systematic investigation was launched by Snoek (1936) at Philips Research Laboratory [2]. At the same time Takai (1937) in Japan was seriously engaged in the research work on the same materials [1]. Snoek's extensive works on ferrites unveiled many mysteries regarding magnetic properties of ferrites. He was particularly looking for high permeability materials of cubic structure. This particular structure for symmetry reasons supports low crystalline anisotropy. He found suitable materials in the form of mixed spinels of the type $MeZnFe_2O_4$, where *Me* stands for metals like *Cu*,Fe, *Mg*, *Ni* or *Mn*, for which permeability were found to be up to 4000 [1-3]. Here after starts the story of *Zn* ferrites. Remarkable properties like high permeability, low loss factor, high stability of permeability with temperature and time, high wear resistance, controlled coercive force, low switching coefficient etc. have aptly placed *Zn* ferrites as highly demandable ferrites to both researchers and manufacturers. Every year great deals of paper are being published on various aspects of ferrites. A large number of scientists and technologists are engaged in research to bring about improvements on the magnetic properties of ferrites.

The sintering process is considered to be one of the most vital steps in ferrite preparation and often plays a dominant role in many magnetic properties. Tasaki *et al.* [4]

studied the effect of sintering atmosphere on permeability of sintered ferrite. They found that high density is one of the factors, which contribute to greater permeability. However, permeability decreased in an atmosphere without O_2 at high sintering temperature where high density was expected. This decrease in permeability is attributed to the variation of chemical composition caused by volatilization of Zn. At low sintering temperature a high permeability is obtained in an atmosphere without O_2 because densification and stoichiometry plays a principal role in increasing permeability. At high sintering temperature the highest permeability is obtained in the presence of O_2 because the effect of decrease of Zn content can then be neglected.

Studying the electromagnetic properties of ferrites, Nakamura [5] suggested that both the sintering density and the average grain size increased with sintering temperature. These changes were responsible for variations in magnetization, initial permeability and electrical resistivity.

High permeability attainment is certainly affected by the microstructure of the ferrites. Roess showed that [6] the very high permeability is restricted to certain temperature ranges and the shapes of permeability versus temperature curves are strongly affected by any inhomogeneity in the ferrite structure.

Leung *et al.* [7] performed a Low-temperature Mössbauer study of a ferrite. They found that for $x \leq 0.5$ the resultant *A*- and *B*- site *Fe*-spin moments have a collinear arrangement, whereas for $x > 0.5$ a non-collinear arrangement of *A*- and *B*-site *Fe*-spin moments exists. An explanation based on the relative strength of the exchange constant J_{AB} and J_{BB} is given to account for this difference.

Rezlescu *et al.* [8] reported that the sintering behaviour and microstructure of the ferrites samples largely affected by PbO addition. PbO significantly reduced the sintering temperatures, thus energy consumption is minimized and material loss by evaporation is minimized [9].

There are two mechanisms in the phenomenon of permeability; spin rotation in the magnetic domains and wall displacements. The uncertainty of contribution from each of the mechanisms makes the interpretation of the experimental results difficult. Globus [10] shows that the intrinsic rotational permeability μ_r and 180^0

wall permeability μ_w may be written as: $\mu_r = 1 + 2\pi M_s^2 / K$ and $\mu_w = 1 + 3\pi M_s^2 D / 4\gamma$, where M_s is the saturation magnetization, K is the total anisotropy, D is the grain diameter and $\gamma \equiv K\delta_w$ is the wall energy.

Rosales *et al.* [11] measured the complex permeability of $Zn_{1-x}Ni_xFe_2O_4$ ferrites with $0.3 \le x \le 0.4$. They show that the relaxation frequency and magnetocrystalline anisotropy constant is related by the equation: $f_x = f_{x0} + AK_1$, where f_{x0} and A are constants.

El-Shabasy [12] studied the DC electrical resistivity of $Zn_xNi_{1-x}Fe_2O_4$ ferrites. He shows that the ferrite samples have semiconductor behaviour where DC electrical resistivity decreases on increasing the temperature. $\rho(T)$ for all samples follows $\rho(T) = \rho_0 \exp(E / k_B T)$, where E is the activation energy for electric conduction and ρ_0 is the pre-exponential constant or resistivity at infinitely high temperature. The DC resistivity, $\rho(T)$, decreases as the *Zn* ion substitution increases. It is reported that *Zn* ions prefer the occupation of tetrahedral (*A*) sites, *Ni* ions prefer the occupation of octahedral (*B*) sites while *Fe* ions partially occupy the *A* and *B* sites. On increasing *Zn* substitution (at *A* sites), the *Ni* ion concentration (at *B* sites) will decrease. This lead to the migration of some *Fe* ions from *A* sites to *B* sites to substitute the reduction in *Ni* ion concentration at *B* sites. As a result, the number of ferrous and ferric ions at *B* sites (which is responsible for electric conduction in ferrites) increases. Consequently ρ decreases on Zn substitution. Another reason for the decrease in ρ on increasing *Zn* ion substitution is that, zinc is less resistive ($\rho = 5.92\ \mu\Omega cm$) than nickel ($\rho = 6.99\ \mu\Omega cm$). The main conductivity mechanism in ferrites is attributed to electron hopping between Fe^{3+} and Fe^{2+} in octahedral sites. Resistivity in spinels is very sensitive to stoichiometry; a small variation of *Fe* content in $Zn_{0.7}Ni_{0.3}Fe_{2+x}O_{4-y}$ results in resistivity variations of $\sim 10^7$. Excess *Fe* can easily dissolve in spinel phase by a partial reduction of *Fe* from $3Fe_2^{3+}O_3$ to $2Fe^{2+}Fe_2^{3+}O_4$ (and $1/2O_2 \uparrow$)[2].

2.2 Magnetic Ordering

The onset of magnetic order in solids has two basic requirements:

(i) Individual atoms should have magnetic moments (spins),

(ii) Exchange interactions should exist that couple them together.

Magnetic moments originate in solids as a consequence of overlapping of the electronic wave function with those of neighboring atoms. This condition is best fulfilled by some transition metals and rare-earths. The exchange interactions depend sensitively upon the inter-atomic distance and the nature of the chemical bonds, particularly of nearest neighbour atoms. When the positive exchange dominates, which corresponds to parallel coupling of neighbouring atomic moments (spins), the magnetic system becomes ferromagnetic below a certain temperature T_C called the Curie temperature. The common spin directions are determined by the minimum of magneto-crystalline anisotropy energy of the crystal. Therefore, ferromagnetic substances are characterized by spontaneous magnetization. But a ferromagnetic material in the demagnetized state displays no net magnetization in zero field because in the demagnetized state a ferromagnetic of macroscopic size is divided into a number of small regions called domains, spontaneously magnetized to saturation value and the directions of these spontaneous magnetization of the various domains are such that the net magnetization of the specimen is zero. The existence of domains is a consequence of energy minimization. The size and formation of these domains is in a complicated manner dependent on the shape of the specimen as well as its magnetic and thermal history. When negative exchange dominates, adjacent atomic moments (spins) align antiparallel to each other, and the substance is said to be anti-ferromagnetic below a characteristic temperature, T_N, called the Néel temperature. In the simplest case, the lattice of an anti-ferromagnet is divided into two sublattices with the magnetic moments of these in anti-parallel alignment. This result is zero net magnetization. A special case of anti-ferromagnetism is ferrimagnetism. In ferrimagnetism, there are also two sublattices with magnetic moments in opposite directions, but the magnetization of the sublattices are of unequal strength resulting in a non-zero magnetization and therefore has net spontaneous magnetization. At the macroscopic level of domain structures, ferromagnetic and ferrimagnetic materials are therefore similar.

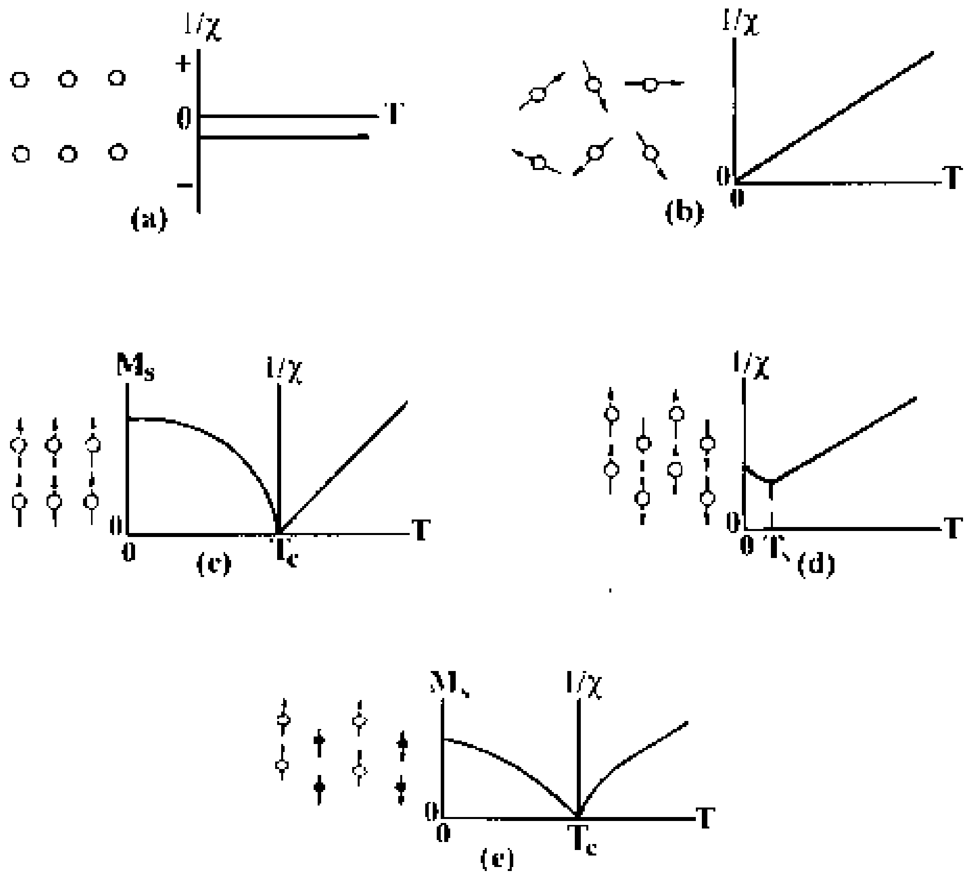

Figure 2.1. Temperature dependence of the inverse susceptibility for: (a) a diamagnetic material; (b) a paramagnetic material, showing Curie's law behaviour; (c) a ferromagnetic material, showing a spontaneous magnetization for $T<T_C$ and Curie-Weiss behaviour for $T>T_C$; (d) an antiferromagnetic material; (e) a ferrimagnetic material, showing a net spontaneous magnetization for $T<T_C$ and non linear behaviour for $T>T_C$. (reproduced from ref. [13]).

The Curie and Néel temperatures characterize a phase transition between the magnetically ordered and disordered (paramagnetic) states. From these simple cases of magnetic ordering various types of magnetic order exists, particularly in metallic substances. Because of long-range order and oscillatory nature of the exchange interaction, mediated by the conduction electrons, structures like helical, conical and modulated patterns might occur. A useful property for characterizing the magnetic materials is the magnetic susceptibility, χ, defined as the magnetization, M, divided by the applied magnetic field, H i.e. $\chi = M/H$. The temperature dependence of susceptibility or, more accurately, inverse of susceptibility is a good characterization parameter for magnetic materials, Fig. 2.1. Fig. 2.1(e) shows that in the paramagnetic region, the variation of the inverse susceptibility with temperature of a ferrite material is decidedly non-linear. Thus the ferrite materials do not obey the Curie-Weiss law, $\chi = C/(T - T_C)$ [2, 13].

2.3 Crystal Structure of Spinel Ferrites

Ferrites have the cubic structure, which is very close to that of the mineral spinel $MgO.Al_2O_3$, and are called cubic spinel. Analogous to the mineral spinel, magnetic spinel have the general formula $MeO.Fe_2O_3$ or $MeFe_2O_4$ where *Me* is the divalent metal ion [14]. This crystal structure was first determined by Bragg and by Nishikawa [1,13]. Formerly, spinels containing *Fe* were called ferrites but now the term has been broadened to include many other ferrimagnets including garnets and hexagonal ferrites these need not necessarily contain iron. The spinel lattice is composed of a close-packed oxygen (radius about 1.3Å) arrangement in which 32 oxygen ions form a unit cell that is the smallest repeating unit in the crystal network. The unit cell of the ideal spinel structures is given in Fig. 2.2. Between the layers of oxygen ions, if we simply visualize them as spheres, there are interstices that may accommodate the metal ions (radii ranging from 0.6 to 0.8Å). Now, the interstices are not all the same: some which we call A sites are surrounded by or coordinated with 4 nearest neighboring oxygen ions whose lines connecting their centers form a tetrahedron. Thus, *A* sites are called tetrahedral sites. The other type of sites (*B* sites) is coordinated by 6 nearest neighbor oxygen ions whose center connecting lines describe an octahedron. The *B* sites are called octahedral sites. In the unit cell of 32 oxygen ions there are 64 tetrahedral sites and 32 octahedral sites. If all these were filled with metal ions, of either +2 or +3 valence, the positive charge would be very much greater than the negative charge and so the structure would not be electrically neutral. It turns out that of the 64 tetrahedral sites, only 8 are occupied and out of 32 octahedral sites, only 16 are occupied. Thus the unit cell contains eight formula units AB_2O_4, with 8 *A* sites, 16 *B* sites and 32 oxygen ions, and total of 8 x 7 = 56 ions. A spinel unit cell contains two types of subcells, Fig. 2.2.

The two types of subcells alternate in a three-dimensional array so that each fully repeating unit cell requires eight subcells, Fig. 2.3.

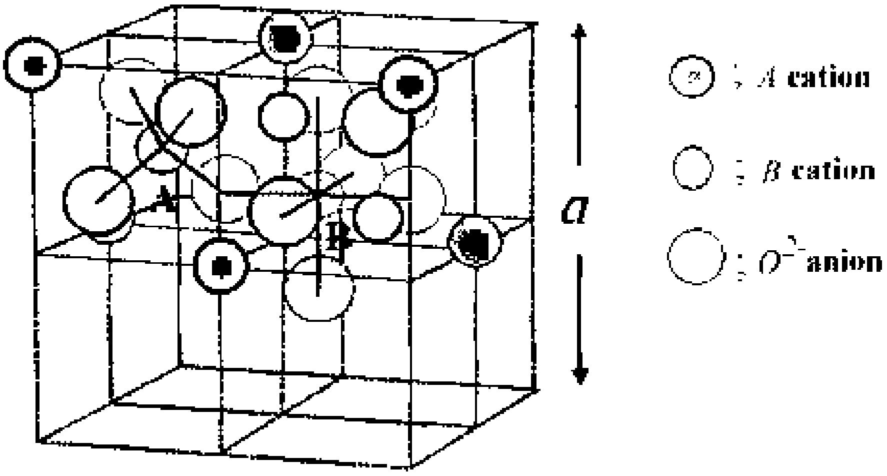

Figure 2.2. Two subcells of a unit cell of the spinel strucrure.

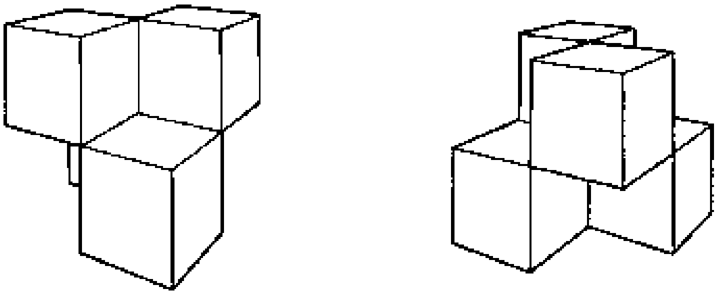

A sites

B sites

Figure 2.3. Unit cell of spinel ferrite divided into eight subcells with *A* and *B* sites.

The positions of the ions in the spinel lattice are not perfectly regular (as the packing of hard spheres) and some distortion does occur. The tetrahedral sites are often too small for the metal ions so that the oxygen ions move slightly to accommodate them. The oxygen ions connected with the octahedral sites move in such a way as to shrink the size the octahedral cell by the same amount as the tetrahedral site expands. The movement of the tetrahedral oxygen is reflected in a quantity called the oxygen parameter, which is the distance between the oxygen ion and the face of the cube edge along the cube diagonal of the spinel subcell. This distance is theoretically equal to $3/8a_0$-where $a_0$is the lattice constant [1].

2.4 Cation Distribution of Spinel Ferrites

In spinel structure the distribution of cations over the tetrahedral or *A* sites and octahedral or *B* sites can be present in a variety of ways. If all the Me^{2+} ions in $Me^{2+}Me_2^{3+}O_4$ are in tetrahedral and all Me^{3+} ions in octahedral positions, the spinel is then called normal spinel. Another cation distribution in spinel exists, where one half of the cations Me^{3+} are in the *A* positions and the rest, together with the Me^{2+} ions are randomly distributed among the *B* positions. The spinel having the latter kind of cation distribution is known as inverse spinel. The distribution of these spinels can be summarized as [2, 15-16]:

1) Normal spinels, i.e. the divalent metal ions are on *A*-sites: $Me^{2+}[Me_2^{3+}]O_4$,
2) Inverse spinels, i.e. the divalent metal ions are on *B*-sites: $Me^{3+}[Me^{2+}Me_2^{3+}]O_4$.

A completely normal or inverse spinel represents the extreme cases. *Zn* ferrites have normal spinel structure and its formula may be written as $Zn^{2+}[Fe^{3+}Fe^{3+}]O_4^{2-}$. There are many spinel oxides which have cation distributions intermediate between these two extreme cases and are called mixed spinels. The general cation distribution for the spinel can be indicated as:

$$(Me_x^{2+}Me_{1-x}^{3+})[Me_{1-x}^{2+}Me_{1+x}^{3+}]O_4$$

where the first and third brackets represent the A and B sites respectively. For normal spinel $x=1$, for inverse spinel $x=0$. The quantity x is a measure of the degree of inversion. In the case of some spinel oxides x depends upon the method of preparation.

The basic magnetic properties of the ferrites are very sensitive functions of their cation distributions. Mixed ferrites having interesting and useful magnetic properties are prepared by mixing two or more different types of metal ions. The chemical formula of mixed *Zn* ferrite may be written as $(Zn_x^{2+}Fe_{1-x}^{3+})[Fe_{1-x}^{2+}Fe_{1+x}^{3+}]O_4^{2-}$ where $0 \leq x \leq 1$.

Spinel oxides are ionic compounds and hence the chemical bonding occurring in them can be taken as purely ionic to a good approximation. The total energy involved, however, consists of the Coulomb energy, the Born repulsive energy, the polarization and the magnetic interaction energy. The energy terms are all dependent on lattice constant, oxygen position parameter and the ionic distribution. In principle the equilibrium cation distribution can be calculated by minimizing the total energy with respect to these variables. But the only energy that can be written with any accuracy is the Coulomb energy. The individual preference of some ions for certain sites resulting from their electronic configuration also play an important role. The divalent ions are generally larger than the trivalent (because the larger charge produces greater electrostatic attraction and so pulls the outer orbits inward). The octahedral sites are also larger than the tetrahedral. Therefore, it would be reasonable that the trivalent ions Fe^{3+} (0.67Å) would go into the tetrahedral sites and the divalent ions Fe^{2+} (0.83Å) go into the octahedral. Two exceptions are found in Zn^{2+} and Fe^{2+} which prefer tetrahedral sites because the electronic configuration is favourable for tetrahedral bonding to the oxygen ions. Thus Zn^{2+} (0.82Å) prefer tetrahedral sites over the Fe^{3+} (0.67Å) ions. Hence the factors influencing the distribution of cations among the two possible lattice sites are mainly their ionic radii of the specific ions, the size of the interstices, temperature, the matching of their electronic configuration to the surrounding anions and the electrostatic energy of the lattice, the so-called Madelung energy, which has the predominant contribution to the lattice energy under the constrain of overall energy minimization and charge neutrality.

2.5 Interaction between Magnetic Moments on Lattice Sites

Spontaneous magnetization of spinels (at 0K) can be estimated on the basis of their composition, cation distribution, and the relative strength of the possible interaction. Since cation-cation distances are generally large, direct (ferromagnetic) interactions are negligible. Because of the geometry of orbital involved, the strongest superexchange interaction is expected to occur between octahedral and tetrahedral cations. The strength of interaction or exchange force between the moments of the two metal ions on different sites depends on the distances between these ions and the oxygen ion that links them and also on the angle between the three ions. The nearest neighbours of a tetrahedral, an octahedral and an anion site are shown in Fig. 2.4. The interaction is greatest for an angle of 180° and also where the interionic distances are the shortest. Fig. 2.5 shows the inteionic distances and the angles between the ions for the different type of interactions. In the *A-A* and *B-B* cases, the angles are too small or the distances between the metal ions and the oxygen ions are too large. The best combination of distances and angles are found in *A-B* interactions.

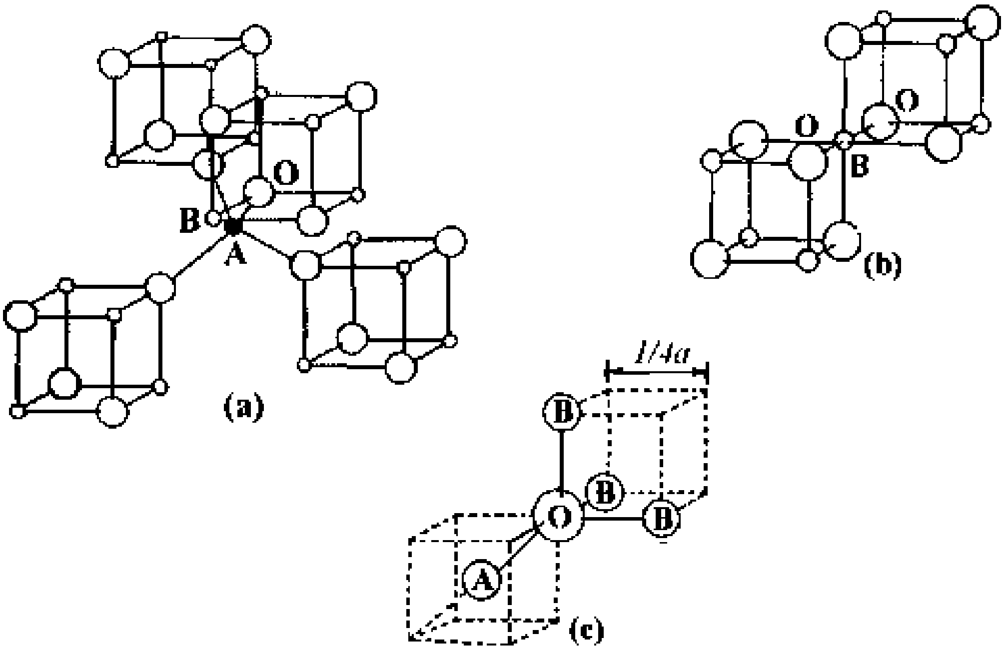

Figure 2.4. Nearest neighbours of (a) a tetrahedral site, (b) an octahedral site and (c) an anion site (taken from ref [2]).

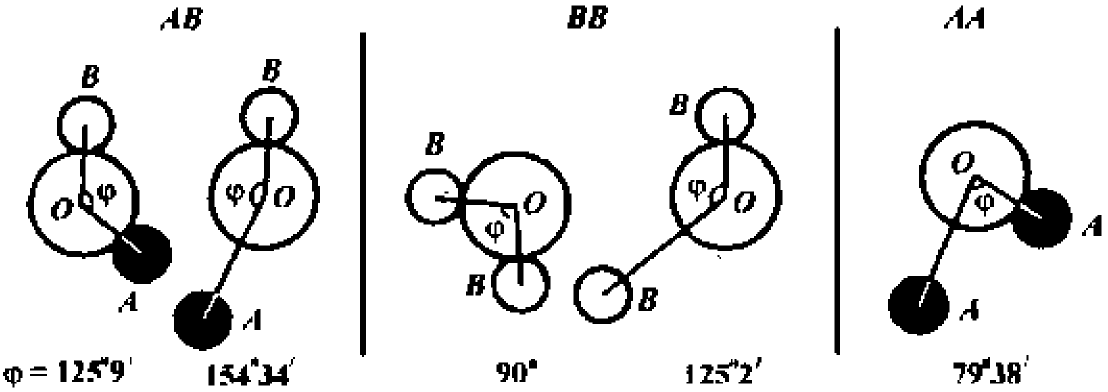

Figure 2.5. Interionic angles in the spinel structure for the different type of lattice site interactions.

For an undistorted spinel, the *A-O-B* angles are about 125^0 and 154^0 [1-2, 17]. The *B-O-B* angles are 90^0 and 125^0 but the latter, one of the *B-B* distances is large. In the *A-A* case the angle is about 80^0. Therefore, the interaction between moments on the *A* and *B* site is strongest. The *BB* interaction is much weaker and the most unfavorable situation occurs in the *AA* interaction. By examining the interaction involving the major contributor, or the *A-B* interaction which orients the unpaired spins of these ions antiparallel, Néel was able to explain the ferrimagnetism of ferrites.

2.6 Magnetism in Spinel Ferrite

The magnetic moment of a free atom is associated with the orbital and spin motions of electrons in an incomplete sub-shell of the electronic structure of the atom. In crystals the orbital motions are quenched, that is the orbital planes may be considered to be fixed in space relative to the crystal lattice, and in such a way that in bulk the crystal has no resultant moment from this source. Moreover this orbital-lattice coupling is so strong that the application of a magnetic field has little effect upon it. The spin axes are not tightly bound to the lattice as are the orbital axes. The anions surrounding a magnetic cation subject it to a strong inhomogeneous electric field and influence the orbital angular momentum. However, the spin angular momentum remains unaffected. For the first transition gronp elements this crystal field effect is intense partly due to the large radius of the 3d shell and partly due to the lack of any outer electronic shell to screen the 3d shell whose unpaired electrons only contribute to the magnetic moment. We have originally defined the magnetic moment in connection with permanent magnets. The electron itself may well be called the smallest permanent magnet [1]. For an atom with a resultant spin quantum number *S*, the spin magnetic moment will be

$$\mu = g\sqrt{S(S+1)}\mu_B$$

where g is the Landé splitting factor and μ_B, known as the Bohr magneton, is the fundamental unit of magnetic moment. The value of g for pure spin moment is 2 and the quantum number associated with each electron spin is $\pm 1/2$. The direction of the moment is comparable to the direction of the magnetization (from South to North poles) of a permanent magnet to which the electron is equivalent. Fig. 2.6 illustrates the electronic configuration of Fe atoms and Fe^{3+} ions. Fe atom has four unpaired electrons and Fe^{3+} ion has five unpaired electrons. Each unpaired electron spin produced 1 Bohr magneton. In compounds, ions and molecules, account must be taken of the electrons used for bonding or transferred in ionization. It is the number of unpaired electrons remaining after these processes occur that gives the net magnetic moment [1]. According to the Hund's rules the moment of Fe atom and Fe^{3+} ion are $4\mu_B$ and $5\mu_B$ respectively. Similarly the moment of Fe^{2+} and Zn^{2+} ion are $4\mu_B$ and $2\mu_B$ respectively.

2.6.1 Exchange Interactions in Spinel

The intense short-range electrostatic field, which is responsible for the magnetic ordering, is the exchange force that is quantum mechanical in origin and is related to the overlapping of total wave functions of the neighbouring atoms.

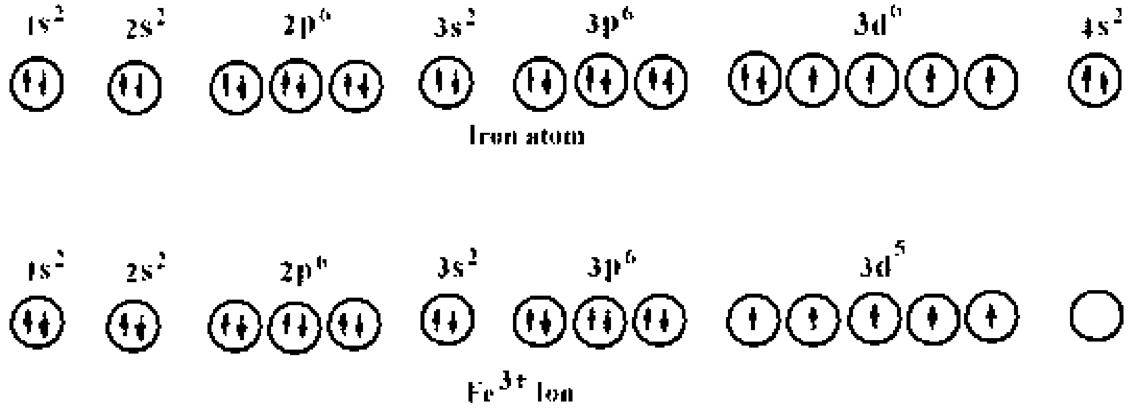

Figure 2.6. Electronic configuration of atoms and ions

The total wave function consists of the orbital and spin motions. Usually the net quantum number is written as S, because the magnetic moments arise mostly due to the spin motion as described above. The exchange interactions coupling the spins of a pair of electrons are proportional to the scalar product of their spin vectors [14, 16, 18],

$$V_{ij} = -2J_{ij}\vec{S}_i \cdot \vec{S}_j \tag{2.1}$$

where J_{ij} is the exchange integral given in a self explanatory notation by

$$J_{ij} = \int \psi_i^*(1)\psi_j^*(2)\left[\frac{1}{r_{12}} + \frac{1}{r_{ij}} - \frac{1}{r_{i1}} - \frac{1}{r_{j2}}\right]\psi_i(2)\psi_j(2)dv_1dv_2 \tag{2.2}$$

In this expression r's are the distances, subscripts i and j refer to the atoms, 1 and 2 refers to the two electrons. If the J in equation (2.1) is positive, we achieve ferromagnetism. A negative J may give rise to anti-ferromagnetism or ferrimagnetism.

Magnetic interactions in spinel ferrites as well as in some ionic compounds are different from the one considered above because the cations are mutually separated by bigger anions (oxygen ions). These anions obscure the direct overlapping of the cation charge distributions, sometimes partially and some times completely making the direct exchange interaction very weak. Cations are too far apart in most oxides for a direct cation-cation interaction. Instead, superexchange interactions appear, i.e., indirect exchange via anion *p*-orbitals that may be strong enough to order the magnetic moments. Apart from the electronic structure of cations this type of interactions strongly depends on the geometry of arrangement of the two interacting cations and the intervening anion. Both the distance and the angles are relevant. Usually only the interactions with in first coordination sphere (when both the cations are in contact with the anion) are important. In the Neél theory of ferrimagnetism the interactions taken as effective are inter- and intra-sublattice interactions *A-B*, *A-A* and *B-B*. The type of magnetic order depends on their relative strength.

The superexchange mechanism between cations that operate via the intermediate anions was proposed by Kramer for such cases and was developed by Anderson and Van Vleck [15, 16]. A simple example of superexchange is provided by *MnO* which was chosen by Anderson. From the crystal structure of *MnO* it will be seen that the antiparallel manganese ions are collinear with their neighbouring oxygen ions. The O^{2-} ions each have six *2p* electrons in three antiparallel pairs. The outer electrons of the Mn^{2+} ions are in *3d* sub-shells which are half filled with five electrons in each. The phenomenon of superexchange is considered to be due to an overlap between the manganese *3d* orbits and the oxygen *2p* orbits with a continuous interchange of electrons between them. It appears that, for the overall energy of the system to be a minimum, the moments of the manganese ions on either side of the oxygen ion must be antiparallel. The manganese magnetic moments are thus, in effect, coupled through the intervening oxygen ion. The idea is illustrated in Fig. 2.7.

In Figs. 2.7(a) and 2.7(c) the outer electrons in a pair of Mn^{2+} ions, and in an intervening O^{2-} ion in the unexcited state, are shown by the arrows. One suggested mode of coupling is indicated in Fig. 2.7(b). The two electrons of a pair in the oxygen ion are simultaneously transferred, one to the left and the other to the right. If their directions of spin are unchanged then, by Hund's rules, the moments of the two manganese ions must be antiparallel as shown. Another possibility is represented in Fig. 2.7(d). One electron only has been transferred to the manganese ion on the left. The oxygen ion now has a moment of $1\mu_B$ and if there is negative interaction between the oxygen ion and the right-hand manganese ion then again the moments of the manganese ions will be antiparallel. If these ideas are accepted then the oxygen ions play an essential part in producing antiferromagnetism in the oxide. Moreover, because of the dumbbell shape of the *2p* orbits, the coupling mechanism should be most effective when the metal ions and the oxygen ions lie in one straight line, that is, the angle between the bonds is 180°, and this is the case with *MnO*.

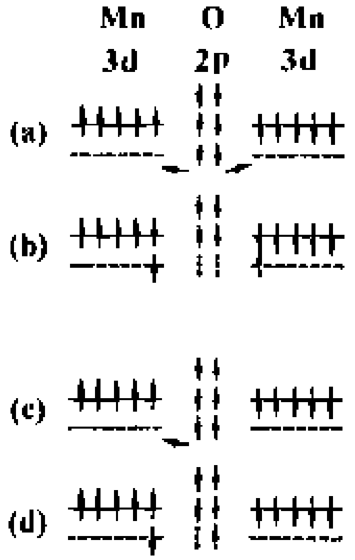

Figure 2.7. Illustrating superexchange in *MnO*.

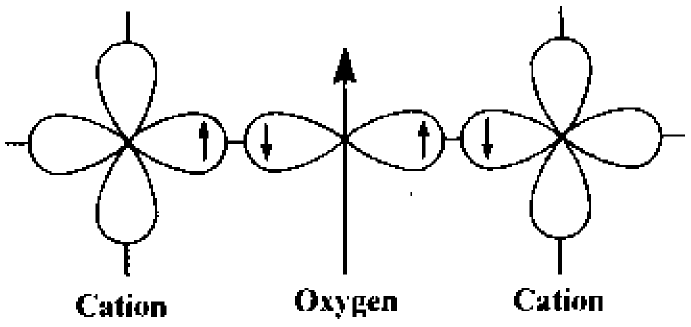

Figure 2.8. Schematic representation of the superexchange interaction in the magnetic oxides.The *p* orbital of an anion (center) interact with the *d* orbitals of the transitional metal cations [2].

In the case of spinel ferrites the coupling is of the indirect type which involves overlapping of oxygen wave functions with those of the neighboring cations. Consider two transition metal cations separated by an *O*, Fig. 2.8.

The O^{2-} has no net magnetic moment since it has completely filled shells, with p-type outermost orbitals. Orbital p_x has two electrons: one with spin up, and the other with spin down, consistent with pauli's exclusion principle. The essential point is that when an oxygen p orbital overlaps with a cation d orbital, one of the p electrons can be accepted by the cations. When one of the transition-metal cations is brought close the O^{2-}, partial electron overlap (between a $3d$ electron from the cation and a $2p$ electron form the O^{2-}) can occur only for antiparallel spins, because electrons with the same spin are repelled. Empty $3d$ states in the cation are available for partial occupation by the O^{2-} electron, with an antiparallel orientation. Electron overlap between the other cation and the O^{2-} then occurs resulting in antiparallel spins and therefore antiparallel order between the cations. Since the p orbitals are linear, the strongest interaction is expected to take place for *cation*–O^{2-}–*cation* angles close to 180^0 [2].

2.6.2 Néel Theory of Ferrimagnetism

If we consider the simplest case of a two-sublattice system having antiparallel and non-equal magnetic moments, the inequality may be due to:

1) different elements in different sites,
2) same element in different ionic states, and
3) different crystalline fields leading to different effective moments for ions having the same spin.

The spins on one sublattice are under the influence of exchange forces due to the spins on the second sublattice as well as due to other spins on the same sublattice. The molecular fields acting on the two sublattices A and B can be written as [2, 13-18]

$$\vec{H}_A = \lambda_{AA}\vec{M}_A + \lambda_{AB}\vec{M}_B,$$

$$\vec{H}_B = \lambda_{AB}\vec{M}_A + \lambda_{BB}\vec{M}_B$$

where $\vec{M}_A$ and $\vec{M}_B$ are the magnetizatious of the two sublattices and λ's are the Weiss constants. Since the interaction between the sublattices is antiferromagnetic, λ_{AB} must be negative, but λ_{AA} and λ_{BB} may be negative or positive depending on the crystal structure and the nature of the interacting atoms. Probably, these interactions are also negative, though they are in general quite small.

Assuming all the exchange interactions to be negative the molecular fields will be then given by

$$\vec{H}_A = -\lambda_{AA}\vec{M}_A - \lambda_{AB}\vec{M}_B ,$$

$$\vec{H}_B = -\lambda_{AB}\vec{M}_A - \lambda_{BB}\vec{M}_B$$

Since in general, λ_{AA} and λ_{BB} are small compared to λ_{AB}, it is convenient to express the strengths of these interactions relative to the dominant λ_{AB} interaction.

Let $\lambda_{AA} = \alpha\lambda_{AB}$

and $\lambda_{BB} = \beta\lambda_{AB}$

In an external applied field $\vec{H}$, the fields acting on A and B sites are

$$\vec{H}_A = \vec{H} - \lambda_{AB}(\alpha\vec{M}_A - \vec{M}_B),$$

$$\vec{H}_B = \vec{H} - \lambda_{AB}(\vec{M}_A - \beta\vec{M}_B)$$

At temperatures higher than the transition temperature, T_N, $\vec{H}_A$, $\vec{M}_A$ and $\vec{M}_B$ are all parallel and we can write

$$\vec{M}_A = \frac{C_A}{T}[\vec{H} - \lambda_{AB}(\alpha\vec{M}_A - \vec{M}_B)], \qquad (2.3)$$

$$\vec{M}_B = \frac{C_B}{T}[\vec{H} - \lambda_{AB}(\vec{M}_A - \beta\vec{M}_B)] \qquad (2.4)$$

where C_A and C_B are the Curie constants for the two sublattices.

$$C_A = N_A g\mu_B^2 S_A(S_A+1)/3K$$

and $$C_B = N_B g\mu_B^2 S_B(S_B+1)/3K$$

N_A and N_B denote the number of magnetic ions on A and B sites respectively and S_A and S_B are their spin quantum numbers. Solving for the susceptibility, χ, one gets [2, 13]

$$\frac{1}{\chi} = \frac{T}{C} - \frac{1}{\chi_0} - \frac{b}{T-\theta}$$

$$\frac{1}{\chi} = \frac{T + (C/\chi_0)}{C} - \frac{b}{T-\theta} \qquad (2.5)$$

where C, χ_0, b and θ are constants for particular substance and are given by

$$C = C_A + C_B$$

$$\frac{1}{\chi_0} = -\frac{1}{C^2}[C_A^2\lambda_{AA} + C_B^2\lambda_{BB} + 2C_A C_B \lambda_{AB}]$$

$$b = \frac{C_A C_B}{C^3}[C_A^2(\lambda_{AA} - \lambda_{BB})^2 + C_B^2(\lambda_{BB} - \lambda_{AB})^2$$

$$-2C_A C_B\{\lambda_{AB}^2 - (\lambda_{AA} + \lambda_{BB})\lambda_{AB} + \lambda_{AA}\lambda_{BB}\}]$$

$$\theta = -\frac{C_A C_B}{C}(\lambda_{AB} + \lambda_{BB}) - 2\lambda_{AB}$$

Equation (2.5) represents a hyperbola, and the physically meaning part of it is plotted in Fig. 2.9. This curvature of the plot of $1/\chi$ versus T is a characteristics feature of a ferrimagnet. It cuts the temperature axis at T_C, called the Ferrimagnetic Curie point. At high temperatures the last term of equation (2.5) become negligible, and reduces to a Curie-Weiss law:

$$\chi = \frac{C}{T + (C/\chi_0)}$$

This is the equation of straight line, shown dashed in Fig. 2.9, to which the $1/\chi$ versus T curve becomes asymptotic at high temperatures.

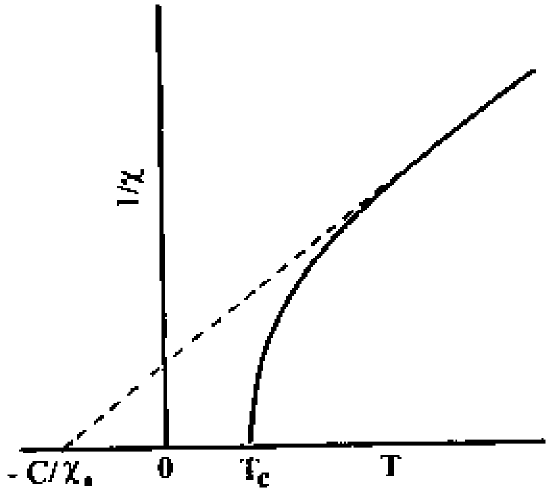

Figure 2.9. The temperature dependence of the inverse susceptibility for ferrimagnets.

The Ferrimagnetic Curie temperature T_C is obtained from equations (2.3) and (2.4) with $H = 0$ and setting the determinant of the coefficients of M_i equal to zero. This gives

$$T_C = \frac{1}{2}[C_A\lambda_{AA} + C_B\lambda_{BB} + \{(C_A\lambda_{AA} - C_B\lambda_{BB})^2 + 4C_AC_B\lambda_{AB}^2\}^2] \qquad (2.6)$$

Equation (2.5) is in good agreement with the experiment, except near the Curie point. The experimental Curie temperature, the temperature at which the susceptibility becomes infinite and spontaneous magnetization appears, is lower than the theoretical Curie temperature [13]. This disagreement between theory and experiment in the region of Curie point is presumably due to the short-range spin order (spin clusters) at temperatures above experimental T_C [2, 13].

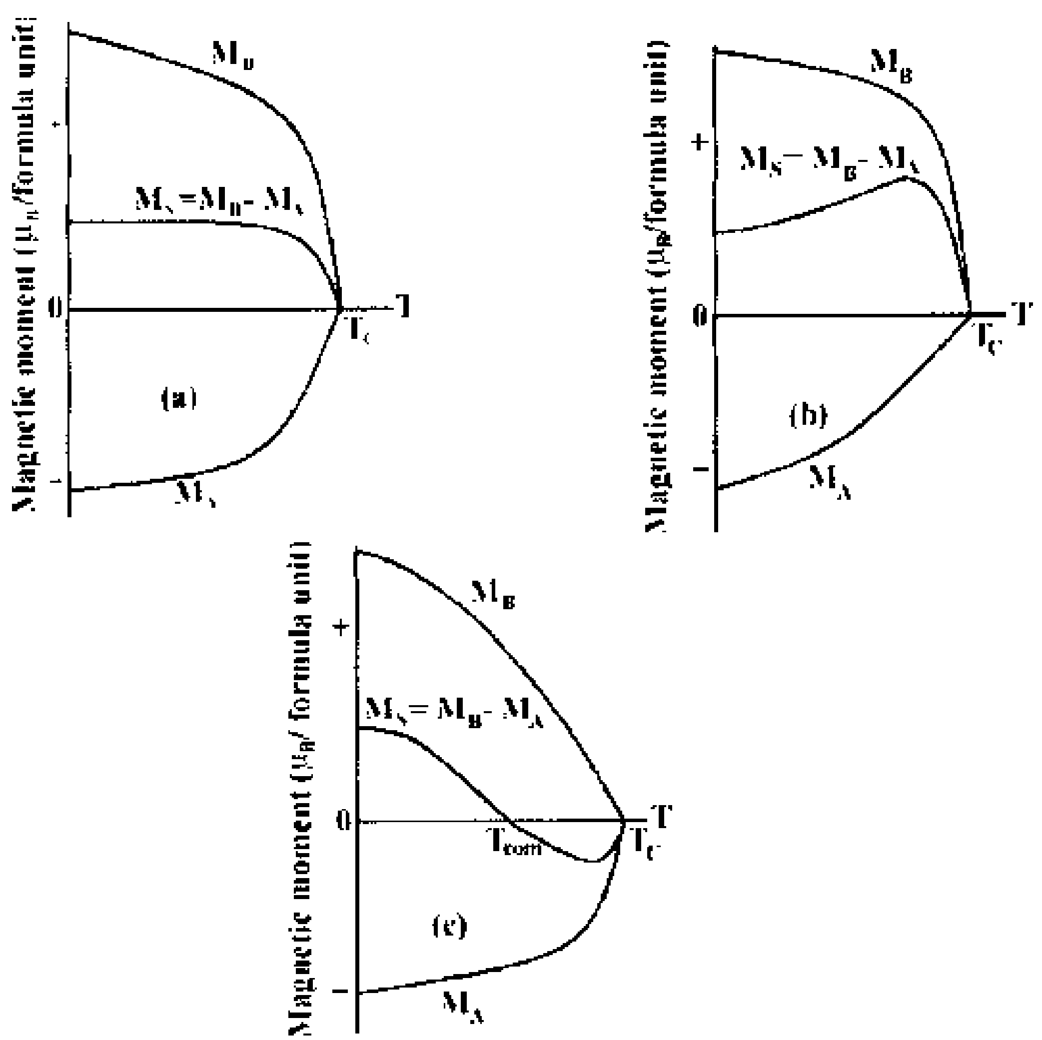

Figure 2.10. Superposition of various combinations of two opposing sublattice magnetizations producing differing resultants including one with a compensation point (schematic).

The sublattice magnetizations will in general have different temperature dependences because the effective molecular fields acting on them are different. This suggests the possibility of having anomaly in the net magnetization versus temperature curves, Fig. 2.10. For most ferrimagnets the curve is similar to that of ferromagnets, but in a few cases there be a compensation point in the curve, Fig. 2.10(c) [1, 13, 14]. At a point below the Curie temperature point, the two sublattice magnetizations are equal and thus appear to have no moment. This temperature is called the compensation point. Below this temperature one sublattice magnetization is larger and provides the net moment. Above this temperature the other magnetization does dominates and the net magnetization reverses direction.

The essential requisite for Néel configuration is a strong negative exchange interaction between *A* and *B* sublattices which results in their being magnetized in opposite directions below the transition point. But there may be cases where intrasublattice interactions are comparable with intersublattice interaction. Neel's theory predicts paramagnetism for such substances at all temperatures. This is unreasonable since strong *AA* or *BB* interaction may lead to some kind of ordering especially at low temperature. In the cases of no *AB* interaction, antiferromagnetic ordering may be expected either in the *A* or in the *B* sublattice. Under certain conditions there may be non-collinear spin arrays of still lower energy.

2.6.3 Effect of Zinc Substitution on the Magnetic Moments in Spinel Ferrites

Fe_3O_4 has ferromagnetic properties because of its inverse structure which leads to the formation of domains. A unit cell of Fe_3O_4 contains eight formula units each of which may be written in the form $Fe^{3+}[Fe^{2+}Fe^{3+}]O_4^{2-}$ [15]. Snoek and his co-workers found that oxides of inverse structure could be artificially produced in which the divalent ions of another element, for example *Mn*,Zn, *Ni*, *Co*, *Mg* or *Cu*, could be substituted for the divalent Fe^{2+} ions in Fe_3O_4. An extensive range of ferrites could thus be made having the general formula $\overset{\rightarrow}{Fe}^{3+}[\overset{\leftarrow}{M}^{2+}\overset{\leftarrow}{Fe}^{3+}]O_4^{2-}$, where arrows indicate spin ordering. Since the trivalent iron ions are equally distributed on *A* and *B* sites they cancel each other out magnetically, and the magnetic moment per formula unit is then theoretically the same as the magnetic moment of the divalent ion. *Zn* ferrite is a normal spinel, with $Zn^{2+}(3d^{10})$ ions in *A* sites have zero magnetic moment; Fe^{3+} ions in *B* sites have a magnetic moment $5\mu_B$. The cation distribution can be written as $Zn^{2+}[\overset{\rightarrow}{Fe}^{3+}\overset{\leftarrow}{Fe}^{3+}]O_4$, where spin ordering is indicated by arrows. The zero magnetic moment of Zn^{2+} ions leaves trivalent iron ions on *B* sites with a negative *BB* interaction between equal ions. Therefore *Zn* ferrite is not ferromagnetic. Zinc ferrite therefore be expected to be antiferromagnetic and thus to have a Néel point, though measurements show it to be paramagnetic only [1,2, 13, 15].

Magnetic properties can be modified widely by cation substitution. An illustrative case is substituion of *Ni* by *Zn* in *Ni* ferrite to form solid solutions $Ni_{1-x}Zn_xFe_2O_4$. The cation distribution can be written as $(Zn_x^{2+}Fe_{1-x}^{3+})[Ni_{1-x}^{2+}Fe_{1+x}^{3+}]O_4^{2-}$ [2]. Zn^{2+} is diamagnetic and its main effect is to break linkages between magnetic cations. Another effect is to increase interaction distance by expanding the unit cell, since it has an ionic radious larger than the *Ni* and *Fe* radii. The most remarkable effect is that substitution of this diamagnetic cation (*Zn*) results in a significant increase in magnetic moment in a number of spinel solid solutions, Fig. 2.11.

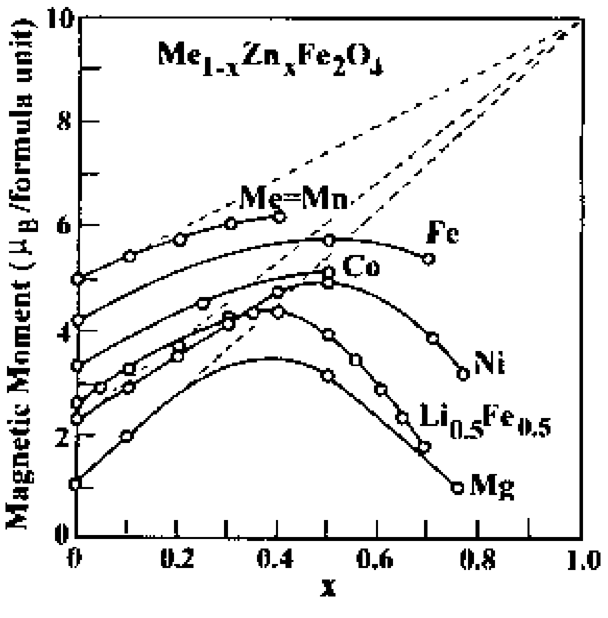

Figure 2.11. Variation of Magnetic moment (in Bohr magnetons per formula unit) with increasing zinc substitution [1, 2].

Magnetic moment as a function of *Zn* content shows an increase for small substitutions, goes through a maximum for intermediate values, decreases and finally vanishes for high *Zn* contents

A simple analysis shows that this increase can be expected for an antiparallel alignment. As the *Zn* content increases, magnetic moments decreases in sublattice *A* and increase in sublattice *B*. If the magnetic moment of *Fe* and *Ni* are 5 and ~2.3 μ_B/ion, respectively, then, per foufumula unit, the total moment in Bohr magnetons on *B* sublattice is $2.3(1-x)+5(1+x)$ and on *A* sublattice the total antiparallel moment is $5(1-x)$. If the resultant moment per formula unit is $M_S(0)$, then by taking the difference of *A* and *B* moments [15],

$$\begin{aligned} M_S(0) &= 2.3(1-x)+5(1+x)-5(1-x) \\ &= x(10-2.3)+2.3 \end{aligned}$$

A linear relationship is obtained with a slope of 7.7, predicting a moment value of $10\mu_B$ per formula unit for *Zn* substitution $x = 1$, as shown by the broken lines in Fig. 2.11. This relationship is not followed over the entire composition range. However, as the *Zn* content increases, $A-O-B$ interactions become too weak and $B-O-B$ interactions begin to dominate. That is, the average distance between the interacting spins gets larger. As a consequence, the system becomes frustrated causing a perturbation to the magnetically ordered spins as large number of *B* sites spins gets non-magnetic impurity atoms as their nearest neighbors.

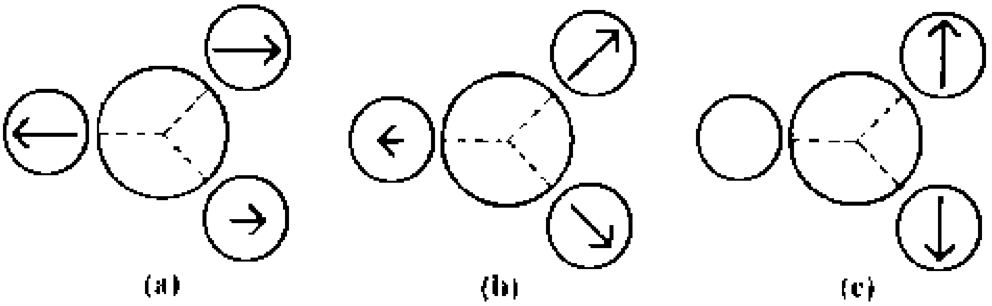

Figure 2.12. Schematic representation of spin arrangements in $Ni_{1-x}Zn_xFe_2O_4$: (a) ferrimagnetic (for $x \le 0.5$); (b) triangular or Yafet-Kittel (for $x > 0.5$); and (c) antiferromagnetic for $x \approx 1$ [2].

The *B* spins are no longer held in place due to this weak anti-ferromagnetic *A*-*B* interaction leading to non-collinearity or canting among the *B* sublattice. Thus for $x > 0.5$ *Zn* content, instead of a collinear antiparallel alignment, canted structure appears, where spins in *B* sites are no longer parallel [16-19], Fig. 2.12. Evidence of this triangular structure has been observed by neutron diffraction [20]; a theoretical analysis showed that departure from collinear order depends on the ratio of the $A-O-B$ to $B-O-B$

molecular field coefficients, $\lambda_{AB} / \lambda_{BB}$ [21]. For high Zn concentration, $B-O-B$ interactions dominant and the ferrite become antiferromagnetic for $x=1$ [2].

2.7 Microstructure

A polycrystal is much more than many tiny crystals bonded together. The interfaces between the crystals, or the *grain boundaries* which separate and bond the grains, are complex and interactive interfaces. The whole set of a given material's properties (mechanical, chemical and especially electrical and magnetic) depend strongly on the nature of the microstructure.

In the simplest case, the grain boundary is the region, which accommodates the difference in crystallographic orientation between the neighbouring grains. For certain simple arrangements, the grain boundary is made of an array of dislocations whose number and spacing depends on the angular deviation between the grains. The ionic nature of ferrites leads to dislocation patterns considerably more complex than in metals, since electrostatic energy accounts for a significant fraction of the total boundary energy [2].

For low-loss ferrite, Ghate [1] states that the grain boundaries influence properties by

1) creating a high ressistivity intergranular layer,
2) acting as a sink for impurities which may act as a sintering aid and grain growth modifiers,
3) providing a path for oxygen diffusion, which may modify the oxidation state of cations near the boundaries.

In addition to grain boundaries, ceramic imperfections can impede domain wall motion and thus reduce the magnetic property. Among these are pores, cracks, inclusions, second phases, as well as residual strains. Imperfections also act as energy wells that pin the domain walls and require higher activation energy to detach. Stresses are microstructural imperfections that can result from impurities or processing problems such as too rapid a cool. They affect the domain dynamics and are responsible for a much greater share of the degradation of properties than would expect [21].

Grain growth kinetics depends strongly on the impurity content. A minor dopant can drastically change the nature and concentration of defects in the matrix, affecting grain boundary motion, pore mobility and pore removal [2, 22]. The effect of a given dopant depends on its valence and solubility with respect to host material. If it is not soluble at the sintering temperature, the dopant becomes a second phase which usually segregates to the grain boundary.

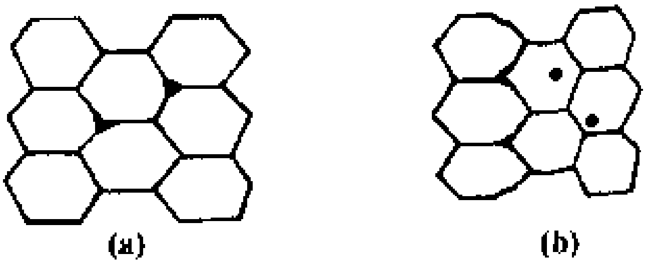

Figure 2.13. Porosity character: (a) intergranular, (b) intragranular.

The porosity of ceramic samples results from two sources, intragranular porosity and intergranular porosity, Fig. 2.13. An undesirable effect in ceramic samples is the formation of exaggerated or discontinuous grain growth which is characterized by the excessive growth of some grains at the expense of small, neighbouring ones, Fig. 2.14. When this occurs, the large grain has a high defect concentration. Discontinuous growth is believed to result from one or several of the following: powder mixtures with impurities; a very large distribution of initial particle size; sintering at excessively high temperatures; in ferrites containing *Zn* a low O_2 partial pressure in the sintering atmosphere. When a very large grain is surrounded by smaller ones, it is called 'duplex' microstructure.

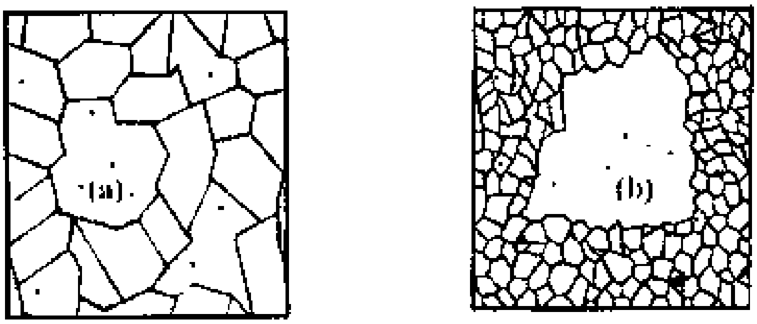

Figure 2.14. Grain growth (a) discontinuous, (b) duplex (schematic) [2].

2.8 Theories of Permeability

Permeability is defined as the proportionality constant between the magnetic field induction B and applied field intensity H [2, 17, 23]:

$$B = \mu H \tag{2.7}$$

If the applied field is very low, approaching zero, the ratio will be called the initial permeability, Fig. 2.15 and is given by

$$\mu_i = \frac{\Delta B}{\Delta H}_{(\Delta H \to 0)}$$

This simple definition needs further sophistications. A magnetic material subjected to an ac magnetic field can be written as

$$H = H_0 e^{i\omega t} \tag{2.8}$$

It is observed that the magnetic flux density B lag behind H. This is caused due to the presence of various losses and is thus expressed as

$$B = B_0 e^{i(\omega t-\delta)} \tag{2.9}$$

Here δ is the phase angle that marks the delay of B with respect to H. The permeability is then given by

$$\mu = \frac{B}{H} = \frac{B_0 e^{i(\omega t-\delta)}}{H_0 e^{i\omega t}} = \frac{B_0 e^{-i\delta}}{H_0} = \frac{B_0}{H_0}\cos\delta - i\frac{B_0}{H_0}\sin\delta = \mu' - i\mu'' \tag{2.10}$$

where
$$\mu' = \frac{B_0}{H_0}\cos\delta \tag{2.11}$$

and
$$\mu'' = \frac{B_0}{H_0}\sin\delta \tag{2.12}$$

The real part (μ') of complex permeability (μ), as expressed in equation (2.10) represents the component of B which is in phase with H, so it corresponds to the normal permeability. If there are no losses, we should have $\mu = \mu'$. The imaginary part μ'' corresponds to that of B, which is delayed by phase angle 90^0 from H [13, 17]. The presence of such a component requires a supply of energy to maintain the alternating magnetization, regardless of the origin of delay. The ratio of μ'' to μ', as is evident from equation (2.12) and (2.11) gives

$$\frac{\mu''}{\mu'}=\frac{\frac{B_0}{H_0}\sin\delta}{\frac{B_0}{H_0}\cos\delta}=\tan\delta \qquad (2.13)$$

This $\tan\delta$ is called loss factor.

The quality factor is defined as the reciprocal of this loss factor, i.e.

$$\text{Quality factor}=\frac{1}{\tan\delta} \qquad (2.14)$$

And the relative quality factor, $Q=\frac{\mu'}{\tan\delta}$ (2.15)

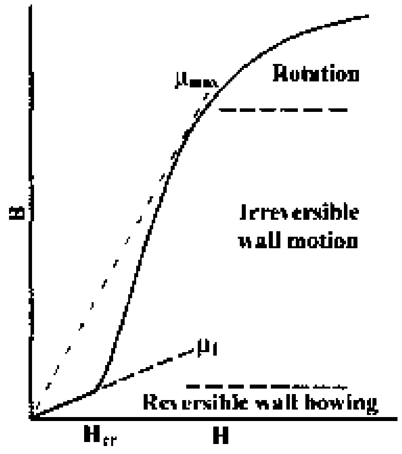

Figure 2.15. Schematic magnetization curve showing the important parameter: initial permeability, μ_i (the slope of the curve at low fields) and the main magnetization mechanism in each magnetization range.

The curves that show the variation of both μ' and μ'' with frequency are called the magnetic spectrum or permeability spectrum of the material [13]. The variation of permeability with frequency is referred to as dispersion. The measurement of complex permeability gives us valuable information about the nature of domain wall and their movements. In dynamic measurements the eddy current loss is very important. This occurs due to the irreversible domain wall movements. The permeability of a ferrimagnetic substance is the combined effect of the wall permeability and rotational permeability mechanisms.

2.8.1 Mechanisms of Permeability

The mechanisms can be explained as follows: A demagnetized magnetic material is divided into number of Weiss domains separated by Bloch walls. In each domain all the magnetic moments are oriented in parallel and the magnetization has its saturation value M_s. In the walls the magnetization direction changes gradually from the direction of magnetization in one domain to that in the next. The equilibrium positions of the walls result from the interactions with the magnetization in neighboring domains and from the influence of pores; crystal boundaries and chemical inhomogeneities which tend to favour certain wall positions.

2.8.1.1 Wall Permeability

The mechanism of wall permeability arises from the displacement of the domain walls in small fields. Lets us consider a piece of material in the demagnetized state, divided into Weiss domains with equal thickness L by means of 180° Bloch walls (as in the Fig. 2.16). The walls are parallel to the YZ plane. The magnetization M_s in the domains is oriented alternately in the $+Z$ or $-Z$ direction. When a field H with a component in the $+Z$ direction is applied, the magnetization in this direction will be favoured. A displacement dx of the walls in the direction shown by the dotted lines will decrease the energy density by an amount [24, 25]:

$$\frac{2M_sH_zdx}{L}$$

This can be described as a pressure M_sH_z exerted on each wall. The pressure will be counteracted by restoring forces which for small deviations may assume to be kdx per unit wall surface. The new equilibrium position is then given by

$$d = \frac{M_sH_zdx}{L}$$

From the change in the magnetization

$$\Delta M = \frac{2M_sd}{L},$$

the wall susceptibility χ_w may be calculated. Let H makes the angle θ with Z direction. The magnetization in the θ direction becomes

$$(\Delta M)_\theta = \frac{2M_s d}{L}\cos\theta \text{, And with } H_z = H\cos\theta \text{ and } d = \frac{2M_s H_z}{K}$$

we obtain

$$\chi_w = \frac{(\Delta M)_\theta}{H} = \frac{4M_s^2\cos^2\theta}{KL} \qquad (2.16)$$

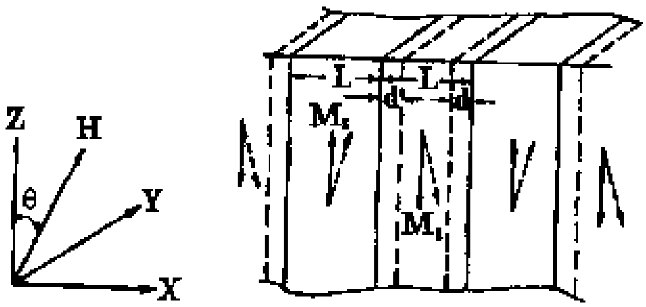

Figure 2.16. Magnetization by wall motion and spin rotation.

2.8.1.2 Rotational Permeability

The rotational permeability mechanism arises from rotation of the magnetization in each domain. The direction of M can be found by minimizing the magnetic energy E as a function of the orientation. Major contribution to E comes from the crystal anisotropy energy. Other contributions may be due to the stress and shape anisotropy. The stress may influence the magnetic energy via the magnetostriction. The shape anisotropy is caused by the boundaries of the sample as well as by pores, nonmagnetic inclusions and inhomogeneities. For small angular deviations, α_x and α_y may be written as

$$\alpha_x = \frac{M_x}{M_s} \text{ and } \alpha_y = \frac{M_y}{M_s}.$$

For equilibrium Z-direction, E may be expressed as [24, 25]

$$E = E_0 + \frac{1}{2}\alpha_x^2 E_{xx} + \frac{1}{2}\alpha_y^2 E_{yy}$$

where it is assumed that x and y are the principal axes of the energy minimum. Instead of E_{xx} & E_{yy}, the anisotropy field H_x^A and H_y^A are often introduced. Their magnitude is given by

$$H_x^A = \frac{E_{xx}}{2M_s} \text{ and } H_y^A = \frac{E_{yy}}{2M_s},$$

H_x^A & H_y^A represent the stiffness with which the magnetization is bound to the equilibrium direction for deviations in the x and y direction, respectively. The rotational susceptibilities $\chi_{r,x}$ and $\chi_{r,y}$ for fields applied along x and y directions, respectively are

$$\chi_{r,x} = \frac{M_s}{H_x^A} \text{ and } \chi_{r,y} = \frac{M_s}{H_y^A}.$$

For cubic materials it is often found that H_x^A and H_y^A are equal. For $H_x^A = H_y^A = H^A$ and a field H which makes an angle θ with the Z direction (as shown in Fig. 2.16) the rotational susceptibility, $\chi_{r,c}$ in one crystallite becomes

$$\chi_{r,c} = \frac{M_s}{H^A}\sin^2\theta \tag{2.17}$$

A polycrystalline material consisting of a large number of randomly oriented grains of different shapes, with each grain divided into domains in a certain way. The rotational susceptibility χ_r of the material has to be obtained as a weighted average of $\chi_{r,c}$ of each crystallite, where the mutual influence of neighbouring crystallites has to be taken into account. If the crystal anisotropy dominates other anisotropies, then H^A will be constant throughout the material, so only the factor $\sin^2\theta$ (equation 2.17) has to be averaged. Snoek [26] assuming a linear averaging of $\chi_{r,c}$ and found

$$\chi_r = \frac{2M_s}{3H^A}$$

The total internal susceptibility

$$\chi = \chi_w + \chi_r = \frac{4M_s^2\cos^2\theta}{KL} + \frac{2M_s}{3H^A} \tag{2.18}$$

If the shape and stress anisotropies cannot be neglected, H^A will be larger. Any estimate of χ_r will then be rather uncertain as long as the domain structure, and the pore distribution in the material are not known. A similar estimate of χ_w would require knowledge of the stiffness parameter k and the domain width L. These parameters are influenced by such factors as imperfection, porosity and crystallite shape and distribution which are essentially unknown.

References

[1] A. Goldman, *Handbook of Modern Ferromagnetic Materials*, Kulwer Acad. Pub, Boston, U.S.A (1999).

[2] R. Valenzuela, *Magnetic Ceramics*, Cambridge University Press, Cambridge (1994).

[3] M. M. Haque, "Influence of additives on the magnetic and electrical properties of iron-excess Mn-Zn ferrites," *M. Phil. Thesis*, BUET, Bangladesh (2000).

[4] J. Tasaki and T. Ito, *Intl. Conf. On Ferrite*, Japan, 1970.

[5] T. Nakamura, "Low-temperature sintering of Ni-Zn-Cu ferrite and its permeability spectra," *Journal of Magnetism and Magnetic Materials*, **168**, 285 (1997).

[6] E. Roess, *Ferrites*, U. of Tokyo Press, Tokyo, 187 (1971).

[7] L. K. Leung, B. J. Evans and A. H. Morrish, "Low-temperature Mössbauer study of a nickel-zinc ferrite: $Zn_{1-x}Ni_xFe_2O_4$," *Phys. Rev. B*, 8, 29 (1973).

[8] N. Rezlescu, E. Rezlescu, C. Pasnicu and M. L. Craus, "Effects of the rare-earth ions on some properties of a nickel-Zinc ferrite," *J. Phys.: Condens. Matter*, 6, 5707 (1994).

[9] E. Rezlescu, L. Sachelarie, P. D. Popa and N. Rezlescu, "Effect of substitution of diavalent ions on the electrical and magnetic properties of Ni-Zn-Me ferrites," *IEEE Transactions on Magnetics*, **36**, 3962 (2000).

[10] A. Globus, *2nd EPS Conf. on Soft Magnetic Materials*, Wolfson Center for Magnetic Technology, Cardiff, Wales, (1975)

[11] M. I. Rosales, E. Amano, M. P. Cuautle and R. Valenzuela, "Impedance spectroscopy studies of Ni-Zn ferrites," *Materials Science and Engineering*, **B49**, 221 (1997).

[12] M. El-Shabasy, "DC electrical properties of Ni-Zn ferrites," *Journal of Magnetism and Magnetic Materials*, **172**, 188 (1997).

[13] B. D. Cullity, *Introduction to Magnetic Materials*, Addison-Wisley Publishing Company, Inc., California (1972).

[14] M. A. Wahab, *Solid State Physics: Structure and Properties of Materials*, Narosa Publishing House, New Delhi (1999).

[15] F. Brailsford, *Physical Principles of Magnetism*, D. Van Nostrand Company Ltd., London (1966).

[16] A. J. Dekker, *Solid State Physics*, Macmillan India Ltd., New Delhi (1998).

[17] S. Chikazumi, *Physics of Magnetism*, Jhon Wiley & Sons, Inc., New York (1966).

[18] C. Kittel, *Introduction to Solid State Physics*, 7th edition, Jhon Wiley & Sons, Inc., Singapore (1996).

[19] A. K. M. Akther Hossain, M. Seki, T. Kawai and H. Tabata, "Colossal magnetoresistance in spinel type $Zn_{1-x}Ni_xFe_2O_4$," *J. Appl. Phys.*, **96**, 1273 (2004).

[20] N. S. Satya Murthy, M. G. Natera and S. I. Youssef, "Yafet-Kittel angles in nickel-zinc ferrites," *Physical Review*, **181**, 969 (1969).

[21] Y. Yafet and C. Kittel, "Antiferromagnetic arrangements in ferrites," *Physical Review*, **87**, 290 (1952).

[22] M. F. Yan and D. W. Johnson, "Impurity induced exaggerated grain growth in Mn-Zn ferrites," *J. Am. Ceram. Soc.*, 61, 342 (1978).

[23] D. Hadfield, *Permanent Magnets and Magnetism*, Jhon Wiley & Sons, Inc., New York (1962).

[24] S. S. Sikder, "Temperature dependence of magnetization and induced magnetic anisotropy of some Fe, Co and Ni-based amorphous ribbons," *Ph. D. Thesis*, BUET, Bangladesh (1999).

[25] K. M. A. Hussain, "Studty of complex permeability and secondary effects in some cobalt and manganese based ferrites," *M. Phil. Thesis*, BUET, Bangladesh (2003).

[26] J. L. Snoek, "Dispersion and absorptions in magnetic ferrites at frequencies above Mc/s," *Physica*, 14, 207 (1948).

CHAPTER 3

SAMPLE PREPARATION AND EXPERIMENTAL TECHNIQUES

3.1 Introduction

A goal common to all the ferrites is the common formation of the spinel structure. Today, the large majority of ferrite powders are made by the conventional Ceramic process or Solid State Reaction method. Most non-conventional process involves producing the powder by a wet method. Among these methods, some are [1]:

1) Co-precipitation
2) Organic precursors
3) Sol-gel synthesis
4) Spray-drying
5) Freeze-drying
6) Combustion synthesis
7) Glass crystallization

In this chapter, we describe the solid state reaction method that is used in this research work.

3.2 Conventional solid state reaction method

In the solid state reaction method, the required composition is usually prepared form the appropriate amount of raw mineral oxides or carbonates by crushing, grinding and milling. The most common type of mill is the ball mill, which consists of a lined pot with hard spheres or rod inside. Milling can be carried out in a wet medium to increase the degree of mixing. This method depends on the solid state inter-diffusion between the raw materials. Solids do not nsually react at room temperature over normal time scales. Thus it is necessary to heat them at higher temperatures for the diffusion length $(2Dt)^{1/2}$ to exceed the particle size, where D is the diffusion constant for the fast-diffusing species, and t is the firing time. The ground powders are then calcined in air or oxygen at a temperature above 1000°C. For some time, this process is continued until the mixture is converted into the correct crystalline phase. The calcined powders are again crushed into fine powders.

The pellets or toroid-shaped samples are prepared from these calcined powders using die-punch assembly or hydrostatic or isostatic pressure. Sintering is carried out in the solid state, at temperature ranging 1100-1400°C, for times of typically 1-40 h and in various atmospheres (e.g. Air, O_2 and N_2) [2-5]. Fig. 3.1 shows, diagrammatically, the stages followed in ferrite preparation.

The general solid state reaction leading to a ferrite $MeFe_2O_4$ may be represented as

$$MeO + Fe_2O_3 \longrightarrow MeFe_2O_4$$

where *Me* is the divalent ions. There are basically four steps in the preparation of ferrite:

1) Preparation of materials to form an intimate mixture with the metal ions in the ratio which they will have in the final product,
2) Heating of this mixture to form the ferrite (often called calcining),
3) Grinding the calcined powders and pressing the fine powders into the required shape, and
4) Sintering to produce a highly densified product.

3.3 Details of calcining, pressing and sintering

Calcining is defined as the process of obtaining a homogeneous and phase pure composition of mixed powders by heating them for a certain time at a high temperature and then allowing it to cool slowly. During the calcining stage, the reaction of Fe_2O_3 with metal oxide (say, MeO or Me'_2O_3) takes place in the solid state to form spinel according to the reactions [6,7]:

$$MeO + Fe_2O_3 \longrightarrow MeFe_2O_4 \text{ (Spinel)}$$

$$2Me'_2O_3 + 4Fe_2O_3 \longrightarrow 4Me'Fe_2O_4 \text{ (Spinel)} + O_2$$

$$Fe_2O_3 + FeO \longrightarrow Fe_3O_4$$

After that *Zn* ions are introduced by

$$(1\text{-}x)Fe_3O_4 + xZnO \longrightarrow Zn_xFe_{3-x}O_4$$

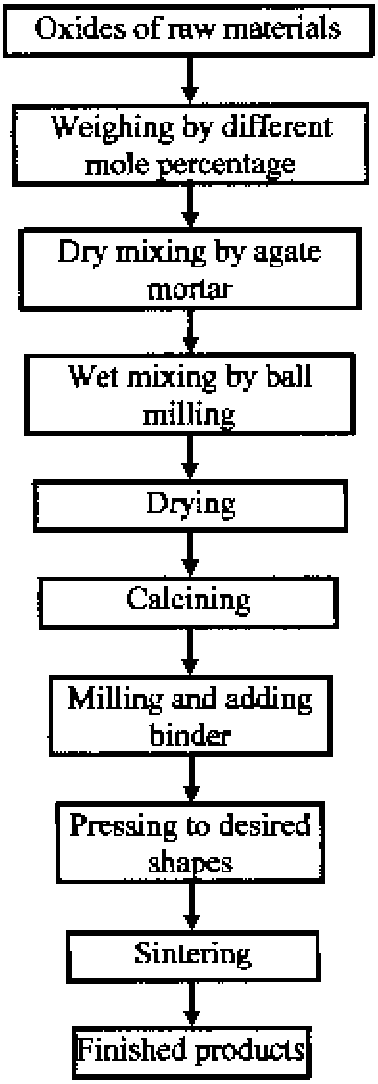

Figure 3.1. Flow chart of the stages in preparation of spinel ferrite.

The calcining process can be repeated several times to obtain a high degree of homogeneity. The calcined powders are crushed into fine powders. The ideal characteristics of fine powders are [6]:

1) small particle size (sub micron)
2) narrow distribution in particle size
3) dispersed particles

4) equiaxed shape of particles
5) high purity
6) homogeneous composition.

A small particle size of the reactant powders provides a high contact surface area for initiation of the solid state reaction; diffusion paths are shorted, leading to more efficient completion of the reaction. Porosity is easily eliminated if the initial pores are very small. A narrow size distribution of spherical particles as well as a dispersed state is important for compaction of the powder during green-body formation. Grain growth during sintering can be better controlled if the initial size is small and uniform.

A binder is usually added prior to compaction, at a concentration lower than 5wt % [6]. Binders are polymers or waxes; the most commonly used binder in ferrite is polyvinyl alcohol. The binder facilitates the particles flow during compacting and increases the bonding between the particles, presumably by forming bonds of the type *particle-binder-particle*. During sintering, binders decompose and are eliminated from the ferrite. Pressures are used for compacting samples vary widely but are commonly several tons per square inch (i. e., up to 10^8 N m^{-2}).

Sintering is defined as the process of obtaining a dense, tough body by heating a compacted powder for a certain time at a temperature high enough to significantly promote diffusion, but clearly lower than the melting point of the main component. The driving force for sintering is the reduction in surface free energy of the powder. Part of this energy is transferred into interfacial energy (grain boundaries) in the resulting polycrystalline body [6, 8]. The sintering time, temperature and the furnace atmosphere play very important role on the magnetic property of ferrite materials. The purposes of sintering process are:

1) to bind the particles together so as to impart sufficient strength to the product,
2) to densify the material by eliminating the pores and
3) to homogenize the materials by completing the reactions left unfinished in the calcining step.

Sintering of crystalline solids is dealt by Coble and Burke [9] who found the following empirical relationship regarding rate of grain growth:

$$\bar{d} = kt^n$$

where $\bar{d}$ is the mean grain diameter, n is about 1/3, t is sintering time and k is a temperature dependent parameter. Sintering is divided into three stages, Fig. 3.2 [6,10-12].

Stage 1. Contact area between particles increases,

Stage 2. Porosity changes from open to closed porosity,

Stage 3. Pore volume decreases; grains grow.

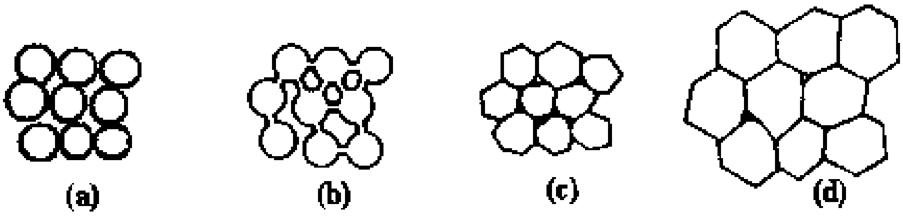

Figure 12. Schematic representation of sintering stages: (a) greenbody, (b) initial stage, (c) intermediate stage, and (d) final stage[2].

In the initial stage, neighbouring particles form a neck by surface diffusion and presumably also at high temperatures by an evaporation-condensation mechanism. Grain growth begins during the intermediate stage of sintering. Since grain boundaries are the sinks for vacancies, grain growth tends to decrease the pore elimination rate due to the increase in distance between pores and grain boundaries, and by decreasing the total grain boundary surface area. In the final stage, the grain growth is considerably enhanced and the remaining pores may become isolated.

3.4 Preparation of the present samples

3.4.1 Collection of beach sand

In Bangladesh, Cox's Bazar beach sand contains potentially valuable minerals as discovered during a geological survey for radioactive minerals in 1961. Beach sand contains magnetic materials in the form of magnetite (Fe_3O_4). Beach sand was collected from Kolatoli sea beach; Cox's Bazar.

3.4.2 Separation of magnetite from the beach sand

The Fe_3O_4 was separated from the beach sand using a strong magnet. At first beach sand are collected from Cox's bazaar sea beach than washed it by water and separated others unnecessary materials such as small rock, shells, clay, etc. Then the sand are dried and finally separated by strong magnet.

3.4.3 Preparation of Fe_3O_4 samples

This magnetite is ground by ball milling for several hours in water media. The coarse powder is eliminated by sedimentation. The raw powders are then sintered at 750 and 900°C for 1 h. X-ray diffraction studies shows that the raw powders sintered at 750°C is the best among these powders. From this dried fine powder of magnetite disk and toroid-shaped (Fig 3.3) samples were prepared by pressing and sintered at various temperatures (750, 850, 900, 950, 975, 1000 and 1200°C) in air for 0.2, 1 and 5h.

3.4.4 Preparation of $Fe_{3-x}Zn_xO4$ samples

Utilizing magnetite from the beach sand and commercially available ZnO, the $Fe_{3-x}Zn_xO_4$ (x = 0.30 and 0.5) ferrites were prepared by a conventional solid state reaction technique. The samples were sintered at 750°C in air for 1 h. The temperature ramp was 10°C/minute for both cooling and heating.

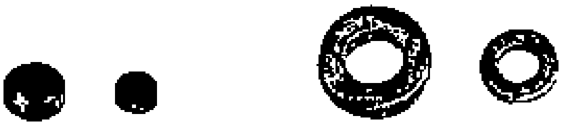
(a) (b)

Figure 3.3. Sample (a) disk shaped, (b) Toroid shaped.

3.5 X-ray diffraction

Bragg reflection is a coherent elastic scattering in which the energy of the X-ray is not changed on reflection. If a beam of monochromatic radiation of wavelength λ is incident on a periodic crystal plane at an angle θ and is diffracted at the same angle as shown in Fig. 3.4, the Bragg diffraction condition for X-rays is given by

$$2d\,Sin\theta = n\lambda \tag{3.1}$$

where d is the distance between crystal planes and n is the positive integer which represents the order of reflection. Equation (3.1) is known as Bragg law. This Bragg law suggests that the diffraction is only possible when $\lambda \le 2d$[11]. For this reason we cannot use the visible light to determine the crystal structure of a material. The X-ray diffraction (XRD) provides substantial information on the crystal structure.

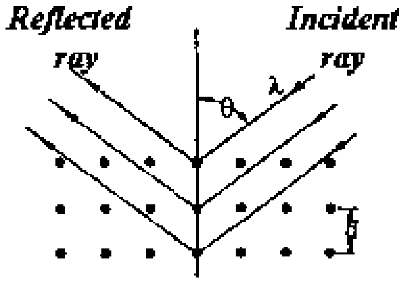

Figure 3.4. Bragg law of diffraction.

X-ray diffraction was carried out with an X-ray diffractometer for the samples. For this purpose monochromatic Cu-K_α radiation was used. The lattice parameter for each peak of each sample was calculated by using the formula

$$a = d\sqrt{h^2 + k^2 + l^2} \tag{3.2}$$

where h, k and l are the indices of the crystal planes. To determine the exact lattice parameter for each sample, Nelson-Riley method was used.

The Nelson-Riley function $F(\theta)$ is given as

$$F(\theta) = \frac{1}{2}\left[\left(Cos^2\theta / Sin\theta\right) + \left(Cos^2\theta / \theta\right)\right] \tag{3.3}$$

The values of lattice constant 'a' of all the peaks for a sample are plotted against $F(\theta)$. Then using a least square fit method exact lattice parameter 'a_0' is determined. The point where the least square fit straight line cut the y-axis (i.e. at $F(\theta) = 0$) is the actual lattice parameter of the sample. The theoretical density ρ_{th} was calculated using following expression:

$$\rho_{th} = \frac{8M}{N_A a_0^3} g/cm^3 \qquad (3.4)$$

where N_A is Avogadro's number (6.02×10^{23} mol^{-1}), M is the molecular weight. The porosity was calculated from the relation $\{100(\rho_{th} - \rho_B)/\rho_{th}\}\%$, where ρ_B is the bulk density measured by the formula $\rho_B = M/V$ [12].

3.6 Microstructural investigation

The micro structural study of the ferrite samples was performed in order to have an insight of the grain structures. The samples of different compositions and sintered at different temperatures were chosen for this purpose. The samples were visualized under a high-resolution optical microscope and then photographed. Average grain sizes (grain diameter) of the samples were determined from optical micrographs by linear intercept technique [2]. To do this, several random horizontal and vertical lines were drawn on the micrographs. Therefore, we counted the number of grains intersected and measured the length of the grains along the line traversed. Finally the average grain size was calculated.

3.7 Complex permeability measurement

For high frequency application, the desirable property of a ferrite is high permeability with low loss. One of the most important goals of ferrite research is to fulfill this requirement. The techniques of permeability measurement and frequency characteristics of the present samples are described in sections 3.7.1 and 3.7.2.

3.7.1 Techniques for the permeability measurement

Measurements of permeability normally involve the measurements of the change in self-inductance of a coil in presence of the magnetic core. The behavior of a self-inductance can now be described as follows. We assume an ideal loss less air coil of inductance L_0. On insertion of a magnetic core with permeability μ, the inductance will be μL_0. The complex impedance Z of this coil [11] can be expressed as follows:

$$Z = R + jX = j\omega L_0 \mu = j\omega L_0(\mu' - j\mu'') \quad (3.5)$$

where the resistive part is $R = \omega L_0 \mu''$ (3.6)

and the reactive part is $X = \omega L_0 \mu'$ (3.7)

The RF permeability can be derived from the complex impedance of a coil, Z, given by equation (3.5). The core is taken as toroidal to avoid demagnetizing effects. The quantity L_0 is derived geometrically as shown in section 3.7.2.

3.7.2 Frequency characteristic measurement

The frequency characteristics of the ferrite samples i.e. the initial permeability spectra were investigated using an Agilent Impedance Analyzer (model no. 4192A). The complex permeability measurements on toroid shaped specimens were carried out at room temperature on all the samples in the frequency range 1 kHz - 13 MHz. The real part (μ_i') and imaginary part (μ_i'') of the complex permeability were calculated using the following relations [1]: $\mu_i' = L_s/L_0$ and $\mu_i'' = \mu_i' \tan\delta$, where L_s is the self-inductance of the sample core and $L_0 = \mu_o N^2 S/\pi\bar{d}$ is derived geometrically. Here L_0 is the inductance of the winding coil without the sample core, N is the number of turns of the coil ($N = 5$), S is the area of cross section of the toroidal sample as given below:

$S = d \times h$,

where $d = \frac{d_2 - d_1}{2}$,

d_1 = Inner diameter,
d_2 = Outer diameter,
h = Height

and $\bar{d}$ is the mean diameter of the toroidal sample as given below:

$$\bar{d} = \frac{d_1 + d_2}{2}$$

The relative quality factor is determined from the ratio $\frac{\mu_i'}{\tan\delta}$.

3.8 DC magnetization measurement

The magnetization (*M*) measurements were made on pieces of the samples (approximate dimensions 2 × 1 × 1 mm^3) using the Superconducting Quantum Interface Device (SQUID) magnetometer (MPMS-5S; Quantum design Co. Ltd.).

References:

[1] A. Goldman, *Handbook of Modern Ferromagnetic Materials*, Kulwer Acad. Pub, Boston, U.S.A (1999).

[2] A. K. M. Akther Hossain, "Investigation of colossal magnetoresistance in bulk and thick film magnetites," *Ph. D. Thesis*, Imperial College, London (1998).

[3] B. D. Cullity, *Introduction to Magnetic Materials*, Addison-Wisley Publishing Company, Inc., California (1972).

[4] R. J. Brook, *Sintering: An Overview, Concise Encyclopedia of Advanced Ceramic Materials*, Pergamon Press, Oxford, pp. 438 (1991).

[5] P. Reijnen, *Science of Ceramics*, Academic Press, London (1967)

[6] R. Valenzuela, *Magnetic Ceramics*, Cambridge University Press, Cambridge (1994).

[7] P. I. Slick, *Ferrites for Non-microwave Applications*, Vol. 2, North Holland Pub. Co. (1980).

[8] W. D. Kingery, H. K. Bowen and D. R. Uhlman, *Introduction to Ceramics*, 2nd edition, Wiley Interscience, Newyork, pp. 476 (1976).

[9] R. L. Coble and J. E. Burke, *4th Int. Symp. On the Reactivity of Solids*, Amsterdam, pp. 38-51 (1960).

[10] I. J. McColm and N. J. Clark, *Forming, Shaping and Working of high Performance Ceramics*, Blackie, Glasgow, pp. 1-338 (1988).

[11] C. Kittel, *Introduction to Solid State Physics*, 7th edition, Jhon Wiley & Sons, Inc., Singapore (1996).

[12] B. D. Cullity, *Introduction to Magnetic Materials*, Addison-Wisley Publishing Company, Inc., California (1972).

CHAPTER 4

RESULTS AND DISCUSSION

The polycrystalline magnetite (Fe_3O_4) separated from Cox's bazaar beach sand and Zn substituted magnetite, $Fe_{3-x}Zn_xO_4$ (x=0.30 and 0.50) were studied. Magnetite powders were separated from the beach sand by a strong magnet. Pellets and ring shaped samples were prepared from this powder. Sample were sintered at various temperatures. The $Fe_{3-x}Zn_xO_4$ (x=0.30 and 0.50) were prepared by mixing magnetite from the beach sand and commercially available ZnO. Internal structure of the above mentioned samples are studied by x-ray diffraction The magnetic properties were studied by SQUID magnetometer. The complex permeability of the samples was characterized with high frequency (1 kHz-13MHz) with an Agilent impedance analyzer. The electrical transport properties of magnetite was investigated by physical property measurement system (PPMS) equipped with 9T magnet and a close cycle helium cryocooler.

4.1 Magnetite separated from the Cox's bazar beach sand

4.1.1 X-ray diffractions and lattice parameters

The X-ray diffraction (XRD) patterns for the separated raw magnetite (Fe_3O_4) from the beach sand and sintered Fe_3O_4 are presented in Figs. 4.1, 4.2 and 4.3 and their diffraction peak positions with Miller indices are presented in Table 4.1. The raw Fe_3O_4 powders were sintered at two different temperatures 750°C and 900°C for 1 hour. The XRD patterns for these raw and sintered samples confirm the formation of spinel ferrite with a few impurity peaks [1,2]. Some of the impurity peaks are perhaps due to the presence of hematite (Fe_2O_3) as shown in the figure. Besides these, some other unidentified peaks are also present in the XRD pattern. This suggests that our magnetic separation process is not sufficient to get phase pure magnetite from the Cox's Bazar beach sand. However, when the raw powder is sintered at 750°C for 1 h, it was observed that some of the impurity peaks are either disappear or become less intense perhaps due to remove some volatile materials. That indicate better crystalline and more pure than raw Fe_3O_4. But when the raw powder sintered at 900°C the impurity peaks are reappear, perhaps due to the formation of Fe_2O_3.

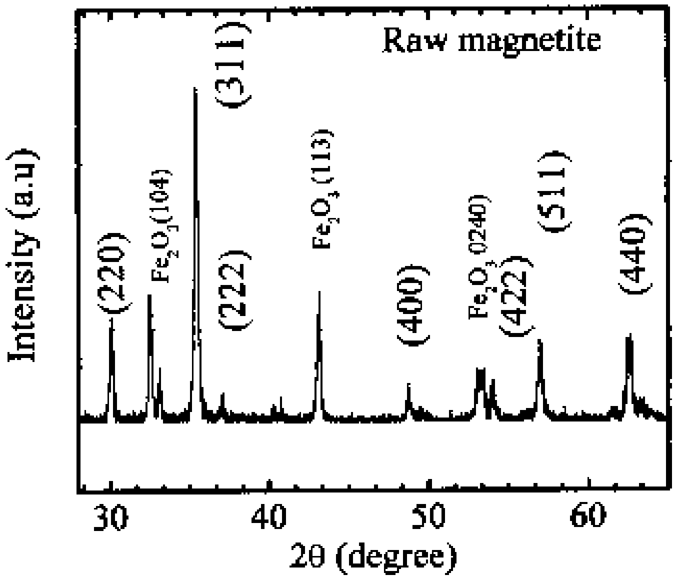

Figure 4.1. The X-ray diffraction pattern of raw magnetite separated from the Cox's Bazar beach sand.

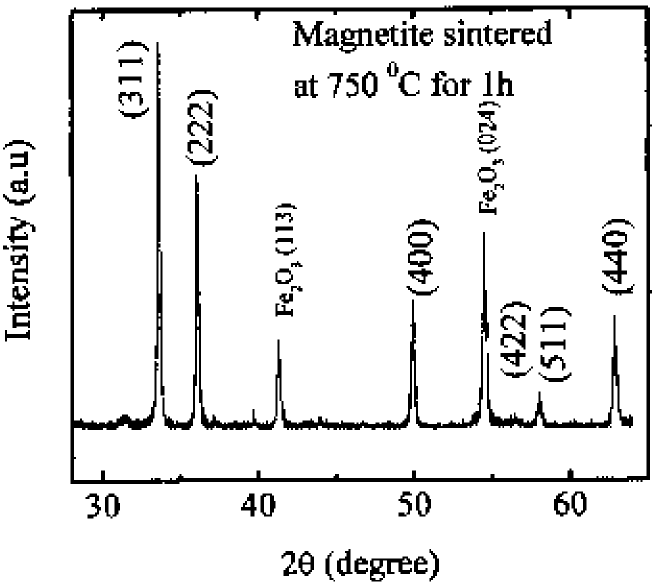

Figure 4.2. The X-ray diffraction pattern of magnetite sintered at 750°C for 1 hour.

Table 4.1. X-ray peak positions for magnetite sintered at 750 °C.

X-ray peak position with Miller indices 2θ (degree)						
Samples	*(220)*	*(311)*	*(400)*	*(422)*	*(511)*	*(440)*
Raw magnetite	30.07	35.40	48.74	56.93	58.60	62.61
Magnetite sintered at 750°C for 1h	-	33.59	49.90	57.99	58.87	60.43
Magnetite sintered at 900°C for 1h	32.06	35.79	46.54	54.06	58.68	62.87

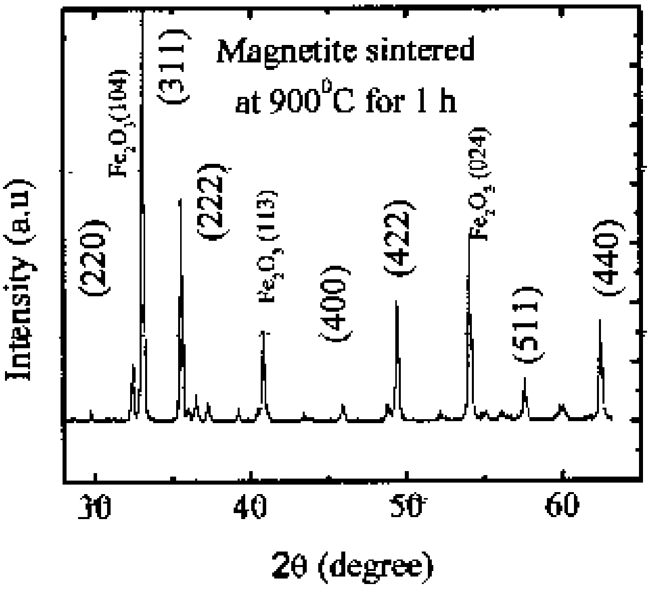

Figure 4.3. The X-ray diffraction pattern of magnetite sintered at 900°C for 1 hour.

The values of lattice parameter '*a*' from all the spinel peaks is plotted against Nelson-Riley function, *F(θ)*, for the sample sintered at 750°C is shown in Figs. 4.4a, b. The calculated *a* and a_0 are presented in Table 4.2. It was found a_0 is 8.403 *(Å)* and 8.405*(Å)* respectively. This value of a_0 agrees well with the value observed by other authors [2,3, 6].

Table 4.2. The lattice parameters and average lattice parameters for magnetite sintered at 900°C for 1 h.

Sample	*peaks*	*Sintering Temp. T,(°C)*	*(Å)*	
			a	*(a_o)*
Magnetite (Fe_3O_4)	1	900	8.378	8.405
	2		8.391	
	3		8.393	
	4		8.394	
	5		8.397	
	6		8.398	
	1	750	8.427	8.403
	2		8.421	
	3		8.419	
	4		8.415	
	5		8.408	

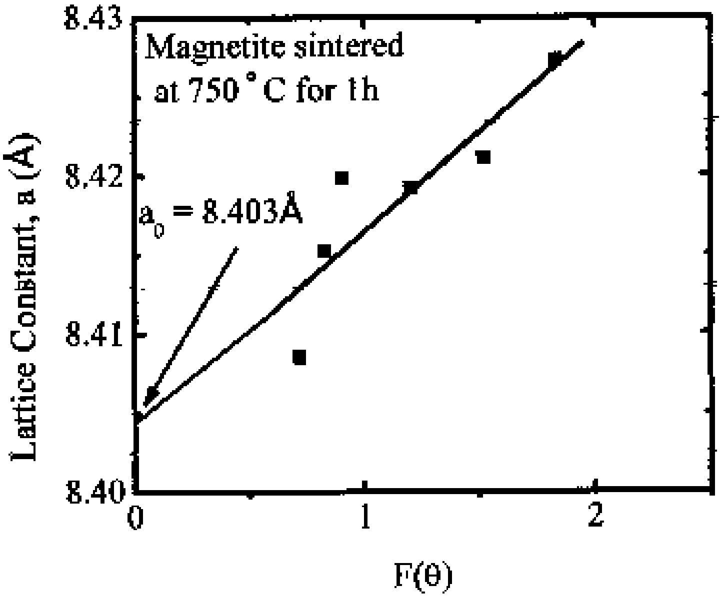

Figure 4.4a. The Nelson- Riley function F(θ) vs lattice constant for the magnetite sintered at 750°C.

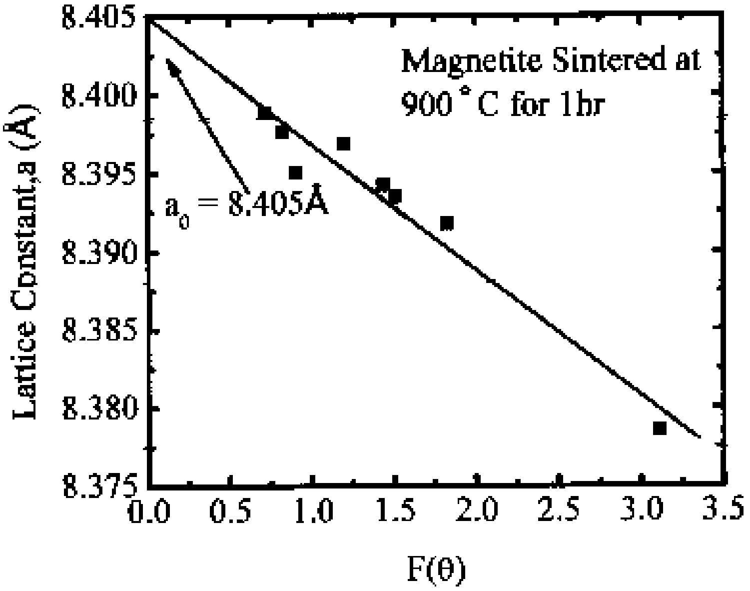

Figure 4.4b. The Nelson- Riley function F(θ) vs lattice constant for the magnetite sintered at 900°C.

4.1.2 Bulk density of the magnetite

From the XRD studies we consider the magnetite powder sintered at 750°C for 1 h is the best powder, hence we use this powder for preparing pellet and ring-shaped samples. Pellet-shaped sample prepared from this powder are again sintered at various temperature and dwell times as presented in Table 4.3. Volume of all samples is measured using Archimedes principle and density is calculated using mass per unit volume.

Table 4.3. Sintering temperature and dwell times for various samples.

Sintering Temperature (°C)	**Dwell times (h)**
750	1
850	1
900	0.2 , 1 and 5
950	0.2 and 1
975	0.2
1000	0.2
1200	0.2

Figs. 4.5, 4.6 and 4.7 show the density as a function of sintering temperatures for the Fe_3O_4. It was observed that the density varies both as a function of sintering temperature and dwell times. From the Fig. 4.6, for fixed dwell time, it was found that the density almost remains same up to sintering temperature 850°C, after this density increases rapidly and at 975°C density approaches approximately 4.6 g/cm^3. On the other hand, at fixed dwell time 0.2 hour (Fig. 4.5) the density for the Fe_3O_4 at 1200°C approaches 4.7 g/cm^3.

At higher sintering temperatures the density inecreases because the intergranular porosity decreases It is known that the porosity of ceramic samples results from two sources, intragranular porosity and intergranular porosity [5]. Thus the total porosity could be written as $P=P_{intra}+P_{inter}$. The intergranular porosity mainly depends on the grain size [5].

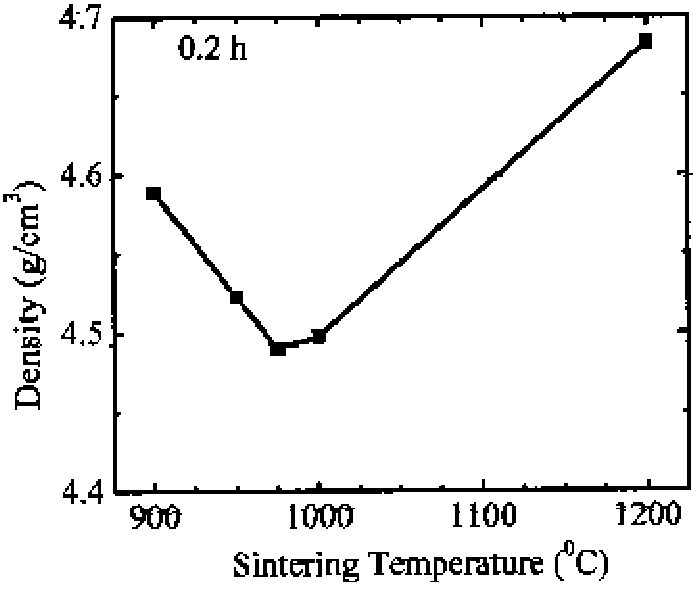

Figure 4.5. Density as a function of sintering temperature for Fe_3O_4 with fixed dwell time 0.2 hour.

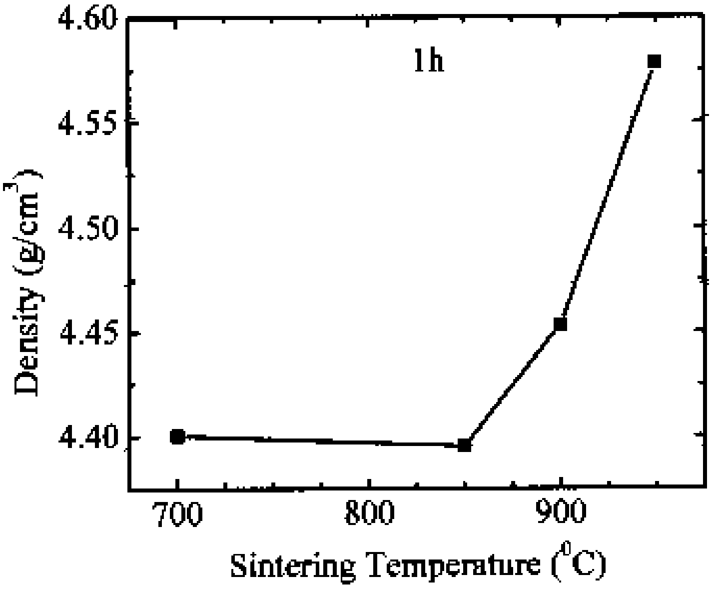

Figure 4.6. Density as a function of sintering temperature for Fe_3O_4 with fixed dwell time 1 hour in air.

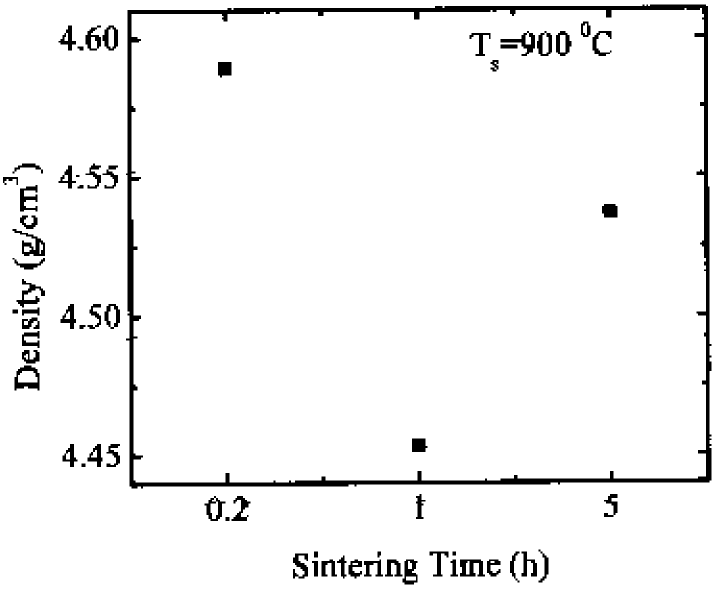

Figure 4.7. Density as a function of sintering time for Fe_3O_4 with fixed temperature.

4.1.3 DC magnetization of magnetite

4.1.3.1 Magnetisation for raw Fe_3O_4

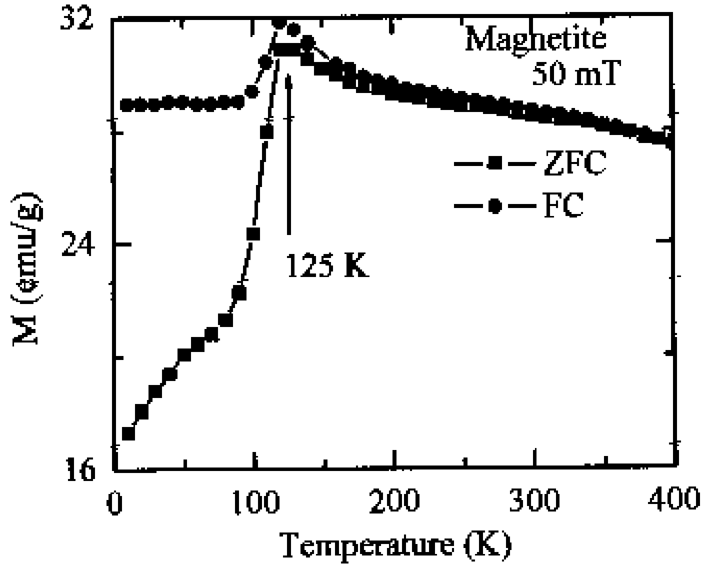

Figure 4.8. The temperature dependence of magnetization for raw magnetite measured in presence of 50 mT applied field in FC and ZFC mode.

The temperature dependent magnetization, M(T), for raw Fe_3O_4 is measured in presence of 50 mT applied field in both zero field cooled (ZFC) mode and field cooled (FC) mode as shown in Fig. 4.8. In ZFC mode the sample is cooled down to 10 K in absence of applied magnetic filed. Then 50 mT field is applied and M(T) data is recorded with warming the sample, while in FC mode M(T) data is recorded in presence of applied magnetic field and cooling the sample.

It was observed that both in ZFC and FC modes sample shows a transition at 125 K. This temperature is called Verwey transition as it was observed by E.W. Verwey while investigating transport properties of single crystal Fe_3O_4 [6,7,8].

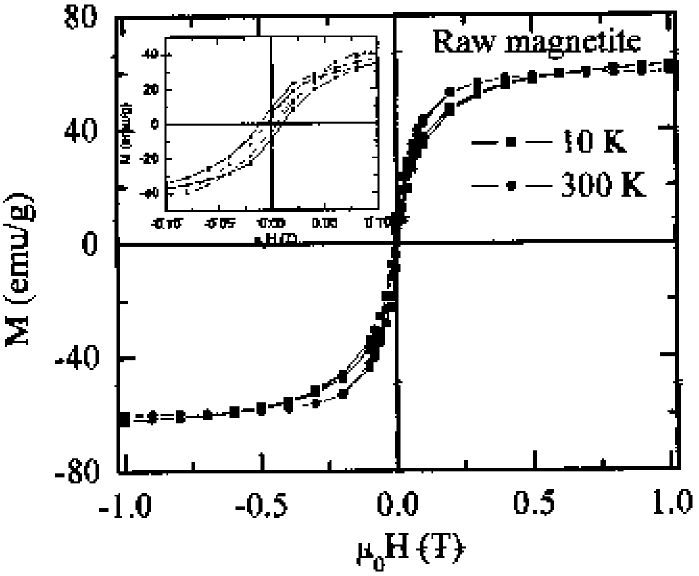

Figure 4.9. The magnetization as a function of applied magnetic field plots for Fe_3O_4 measured at 10K and 300 K.

The magnetization as a function of applied magnetic field, *M(H)*, for raw magnetite is measured both at room temperature (300K) and 10K as shown in Fig. 4.9. The magnetization of Fe_3O_4 increases linearly with increasing the applied magnetic field up to 0.2 T at both the temperatures and attains its saturation value for fields higher than 0.2 T. The 98% of saturation is observed at 0.3 T applied magnetic filed. The saturation magnetization at 10 K for raw Fe_3O_4 is 62.5 emu/g.

The number of μ_B per formula unit is calculated from the experimental values of M_s using following relation,

$$n = \frac{M \times M_s}{N \times \mu_B}, \qquad \text{(Eq.1)}$$

Where M is the molecular weight of the specimen, N is Avogadro's number, and μ_B is 9.27×10^{-21} emu. It was observed that the for the raw Fe_3O_4 the saturation magnetization at 10 K is 2.61 μ_B.

Fe_3O_4 is a ferrimagnetic iron oxide having cubic inverse spinel structure with oxygen anions forming a fcc closed packing and iron (cations) located at the interstitial tetrahedral sites and octahedral sites. The electron can hop between

Fe^{2+} and Fe^{3+} ions in the octahedral sites at room temperature imparting half metallic property to magnetite. The magnetic moment of the unit cell comes only from Fe^{2+} ions with a magnetic moment of $4\mu_B$

4.1.3.2 Magnetisation of Fe_3O_4 sintered at 750°C

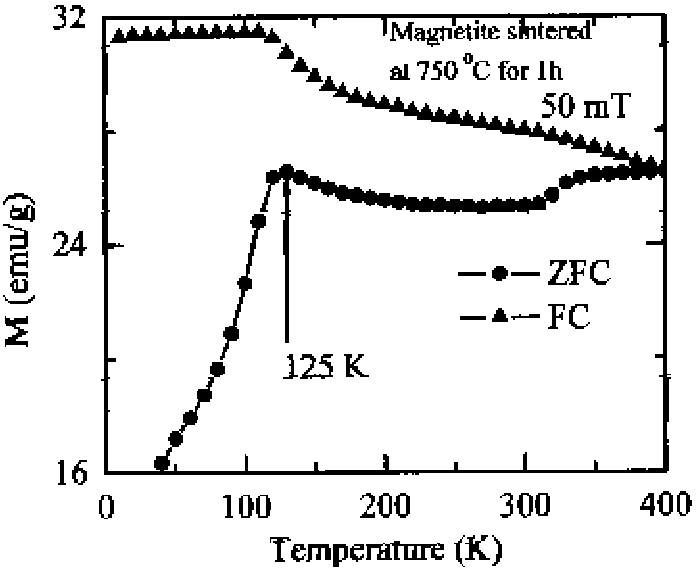

Figure 4.10. The temperature dependent magnetization for sintered magnetite (750°C) measured in presence of 50 mT applied field in *FC* and ZFC mode.

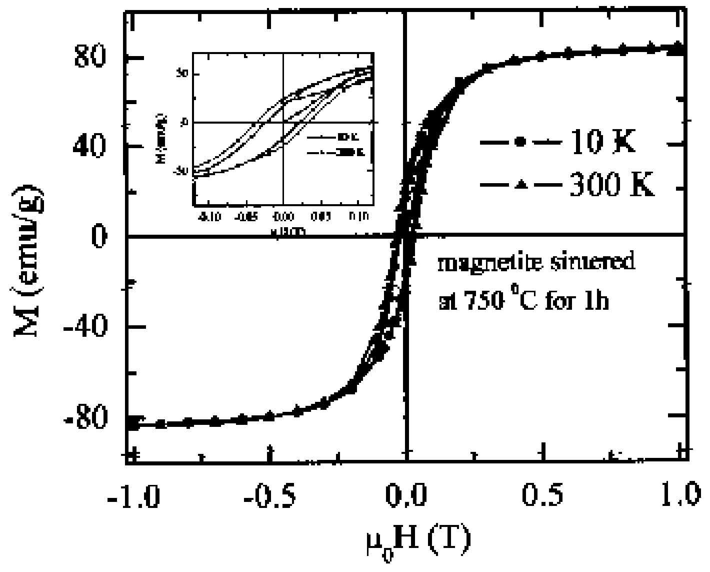

Figure 4.11. The magnetization as a function of applied magnetic field plots for sintered (750°C) Fe_3O_4 measured at 10K and 300 K.

The ZFC and FC M(T) plots for the magnetite sintered at 750 °C is shown in Fig. 4.10. Like raw Fe_3O_4 this sintered sample also exhibit Verwey transition at 125 K. Unlike raw Fe_3O_4, this sample show slightly different behavior in ZFC curve.

The *M(H)* plots for the magnetite sintered at 750°C is measured both at room temperature (300K) and 10K as shown in Fig. 4.11. The magnetization of Fe_3O_4 increases linearly with increasing the applied magnetic field up to 0.2 T at both the temperatures and attains its saturation value for fields higher than 0.2 T. The 98% of saturation is observed at 0.3 T applied magnetic filed. The saturation magnetization at 10 K for this sintered Fe_3O_4 is 83.5 emu/g. This saturation magnetization is corresponds to 3.5 μ_B.

It was found that due to sintering saturation magnetization value increases significantly as a result of sintering., However, present value is less than that of the saturation magnetization value (4 μ_B) of single crystal Fe_3O_4. For this sample the saturation magnetization value is about 88 % of the phase pure Fe_3O_4.

4.1.4 Complex initial permeability of Fe_3O_4

4.1.4.1 Permeability spectra for Fe_3O_4 sintered at various temperatures for 0.2 h

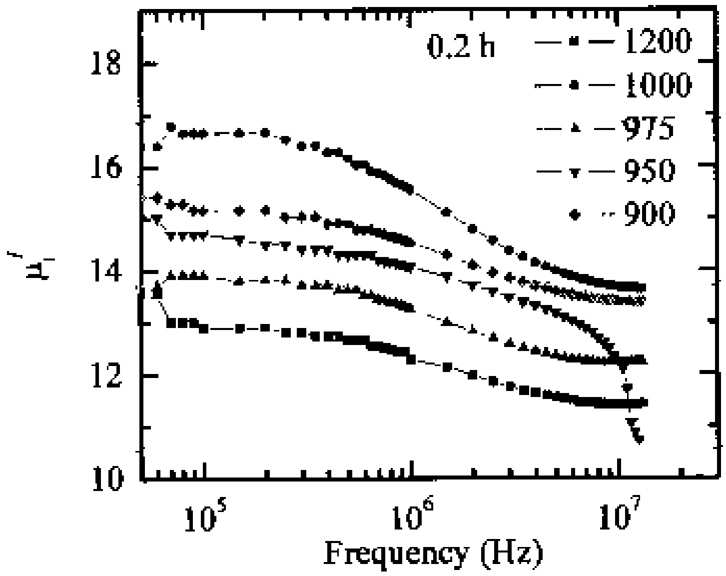

Figure 4.12. The μ_i' spectra for Fe_3O_4 sintered at various temperatures for 0.2hr in air.

Figs. 4.12 and 4.13 show the complex initial permeability spectra for Fe_3O_4 samples sintered at various temperatures for a fixed dwell time 0.2h in the frequency range 100 kHz – 13 MHz. There is slight variation of the real part of the initial permeability, μ_i', (Fig. 4.12) depending on sintering temperature. Among these samples, μ_i' is highest for the sample sintered at 1000°C. Only the sample sintered at 950°C show the resonance frequency in the measured frequency range. For other samples, resonance frequency is beyond 13 MHz.

There is a sharp decrease of μ_i' and an increase of imaginary part of the initial permeability, μ_i'', (Fig. 4.13) above the resonance frequency.

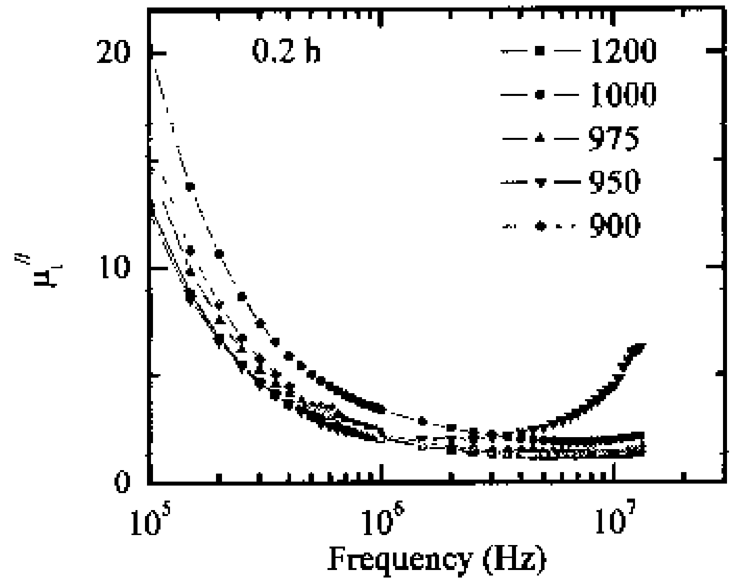

Figure 4.13. The μ_i'' spectra for Fe_3O_4 sintered at various temperatures for 0.2hr in air.

4.1.4.2. Permeability spectra for Fe_3O_4 sintered at various temperatures for 1 h

Figs. 4.14 and 4.15 show the permeability μ_i' and μ_i'' spectra for Fe_3O_4 samples sintered at various temperatures for 1 h respectively. Like the sample sintered for 0.2h, these samples also show a variation of μ_i' depending on sintering temperatures. Compared to the sample sintered for 0.2h, these samples have higher value of μ_i'. In this case, μ_i' is highest for the sample sintered at 750°C. As there is no peak or increasing tendency of μ_i'' (Fig. 4.15) with respect to frequency, it is concluded that the resonance frequency is beyond the measured frequency range.

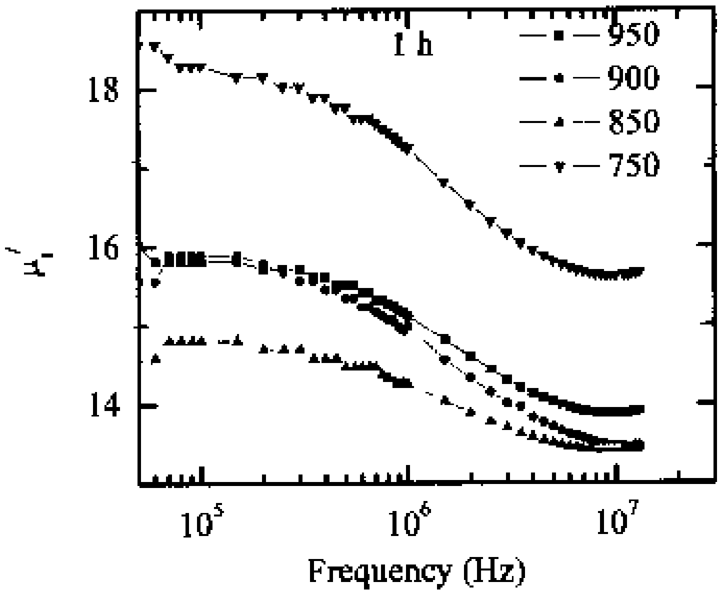

Figure 4.14. The μ_i' spectra for for Fe_3O_4 sintered at various temperatures for 1hr in air.

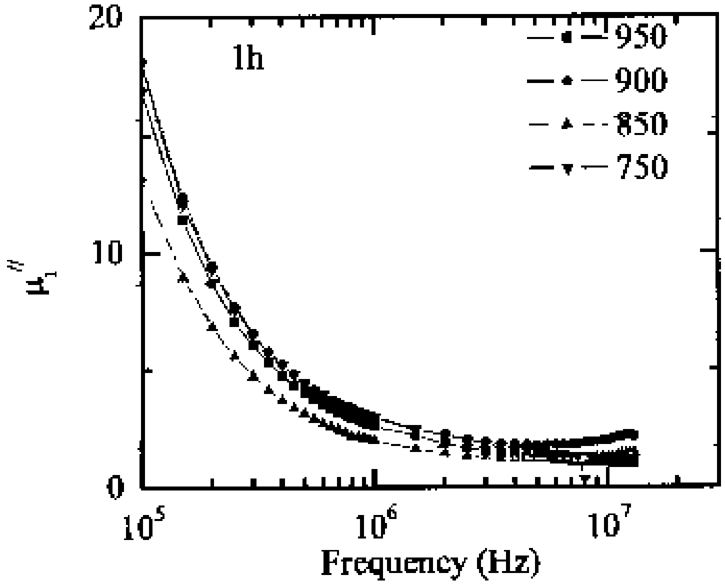

Figure 4.15. The μ_i'' spectra for Fe_3O_4 sintered at various temperatures for 1hr in air.

4.1.4.3. Permeability spectra for Fe_3O_4 sintered at 900°C for various dwell times

Figs. 4.16 and 4.17 show the μ_i' and μ_i'' spectra for Fe_3O_4 samples sintered at 900°C for various dwell times, respectively. It is observed that for a fixed sintering temperature, if furnaces soak time increases then μ_i' values increases and μ_i'' decreases.

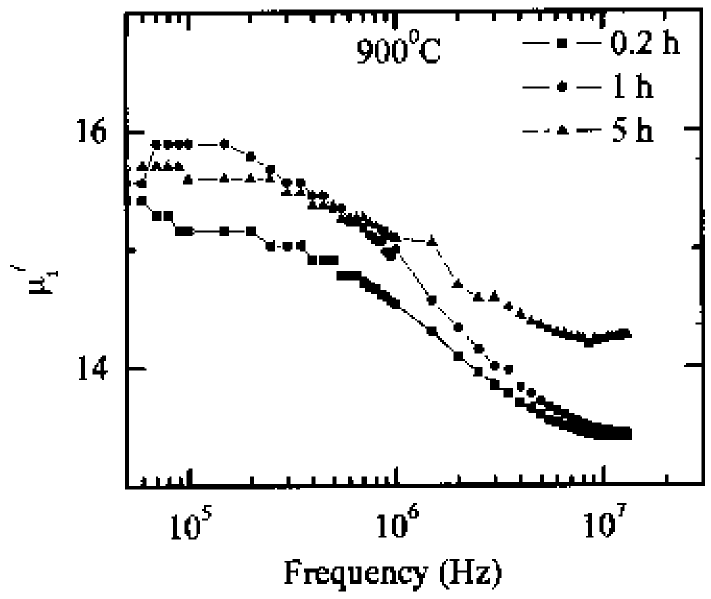

Figure 4.16. The μ_i' spectra for for Fe_3O_4 sintered at 900°C for various dwell times.

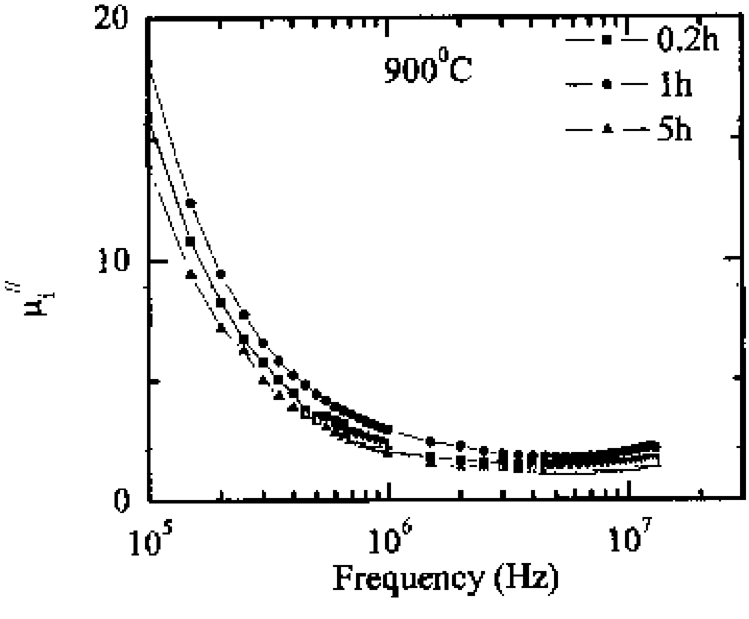

Figure 4.17. The μ_i'' spectra for Fe_3O_4 sintered 900°C for various dwell times.

It is well known that the permeability of ferrite is related to two different magnetizing mechanisms: spin rotation and domain wall motion [9, 10], which can be described as follows:

$$\mu_i = 1 + \chi_w + \chi_{spin}$$

where χ_w is the domain wall susceptibility; χ_{spin} is intrinsic rotational susceptibility. χ_w and χ_{spin} may be written as : $\chi_w = 3\pi M_s^2 D/4\gamma$ and $\chi_{spin} = 2\pi M_s^2/K$ with M_s saturation magnetization, K the total anisotropy, D the average grain diameter, and γ the domain wall energy. Thus the domain wall motion is affected by the grain size and enhanced with the increase of grain size. The initial permeability is therefore a function of grain size. The magnetization caused by domain wall movement requires less energy than that required by domain rotation. As the number of walls increases with the grain sizes, the contribution of wall movement to magnetization increases.

If H is a weak alternating field of high frequency, the domain wall will oscillate back and forth through small distances about their mean position. The differential equation for oscillating boundaries can be written as $md^2x/dt^2 + \beta dx/dt + \alpha x = 2M_s H(t)$, where m is the effective wall mass, β the viscous damping factor, α the restoring constant, x the wall displacement and $H(t)$ the driving force [11, 12]. The first term on the left hand side represents the wall inertia as a product of mass times acceleration; the second term is the damping opposing the propagation velocity, and the third term is associated with wall pinning to defects, expressed as a restoring force. It is also observed that the higher the permeability of the material, the lower the frequency of the onset of ferrimagnetic resonance. This really confirms with Snoek's limit $f_r\mu_i' = \text{Constant}$ [13], where f_r is the resonance frequency for domain wall motion above which μ_i' decreases. This means that there is an effective limit to the product of resonance frequency and permeability so that high frequency and high permeability are mutually incompatible.

Energy loss is an extremely important subject in soft ferrimagnetic materials, since the amount of energy wasted on process other than magnetization can prevent the AC applications of a given material. The ratio of μ_i' and μ_i'' representing the losses in the material are a measure of the inefficiency of the magnetic system. Obviously this parameter should be as low as possible. The magnetic losses, which cause the phase shift, can be split up into three components: hysteresis losses, eddy current losses and residual losses. This gives the formula $\tan\delta_m = \tan\delta_h + \tan\delta_e + \tan\delta_r$. μ_i is the initial permeability which created at low field. Hysteresis losses vanish at very low field strengths. Thus at low field the remaining magnetic losses are eddy current losses and residual losses. Residual losses are independent of frequency. Eddy current losses increase with frequency and are negligible at very low frequency. Eddy current loss can be expressed as $P_e \approx f^2/\rho$, where P_e is the energy loss per unit volume and ρ is the resistivity [14]. To keep the eddy current losses constant as frequency is increased; the resistivity of the material chosen must increase as the square of frequency. Eddy currents are not problem in the ferrites until higher frequencies are encountered because they have very high resistivity about $10^5\Omega cm$ [15]. The ferrite microstructure is assumed to consist of grains of low resistivity separated by grain boundaries of high resistivity. Thicker grain boundaries are preferred to increase the resistance.

4.1.4.4. Quality factor for Fe_3O_4

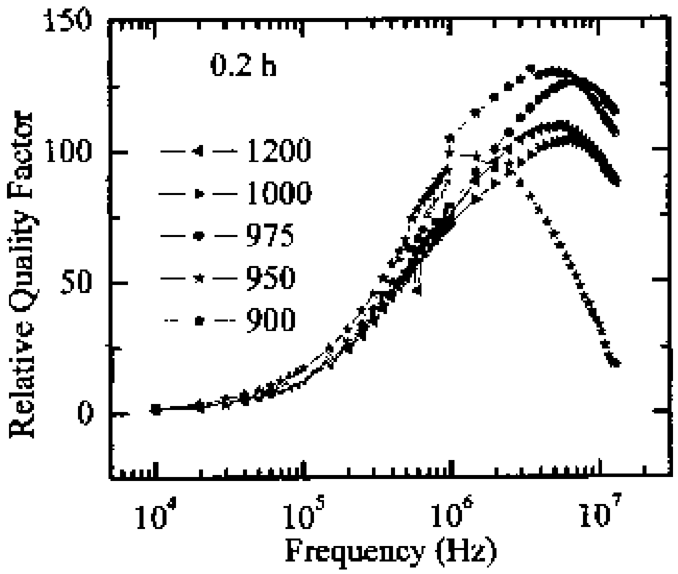

Figure 4.18 The variation of Q factors with frequency for Fe_3O_4 sintered at different temperature for 0.2h.

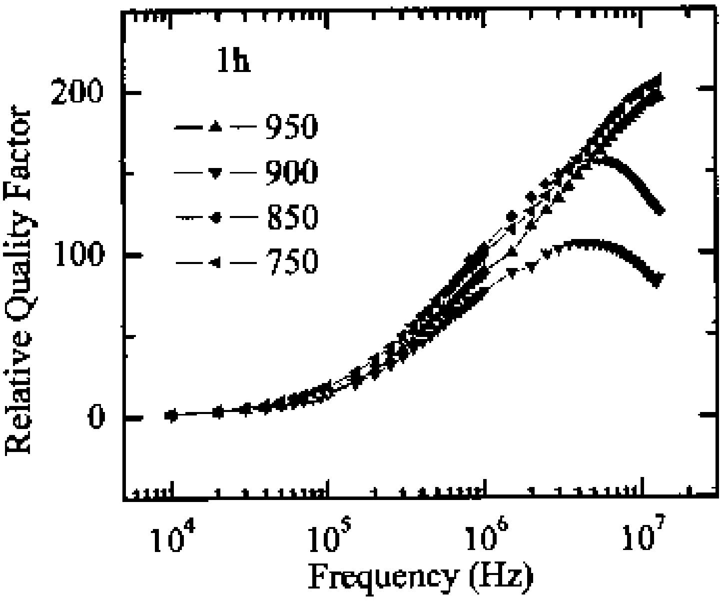

Figure 4.19 The variation of Q factors with frequency for Fe_3O_4 sintered at different temperature for1h.

From the loss factor we have calculated the relative quality factor (or Q factor) for all samples sintered at various temperatures and various dwell times. The Q factors are shown in Fig. 4.18, 4.19 and 4.20. For inductors used in filter applications, the quality factor is often used as a measure of performance. It is observed that the Fe_3O_4 sintered at 750°C for 1 h has the highest Q value (200).

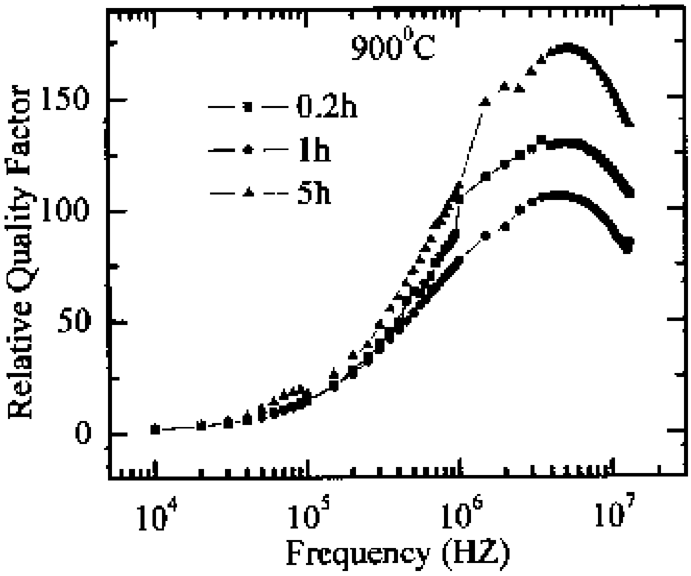

Figure 4.20 The variation of Q factors with frequency for Fe_3O_4 sintered at 900°C for various dwell times.

4.3.4 Transport properties of Magnetite

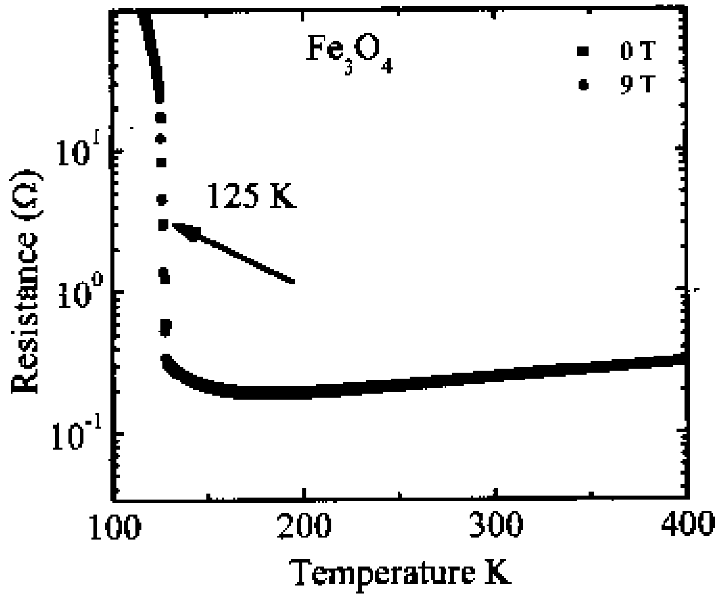

Figure 4.21 The variation of resistance with temperature for Fe_3O_4 sintered at 750°C for 1 h.

Resistance of magnetite sample sintered at 750°C for 1 h is shown in Fig. 4.21. Resistance of the sample is measured at zero field and also in the presence of 9 T magnetic field. Both measurements show that there is a transition in the R-T plots at about 125 K. This is known as famous Verwey transition or electron ordering transition. Similar type of transition is also observed in M(T) measurement at the same temperature for Fe_3O_4 sample.

An electron-ordering transition occurring in a mixed-valent system (Fe^{2+}/Fe^{3+}) that results in an ordering of formal valence states in the low-temperature phase. Example: The prototype system, first identified by Verwey, is the spinel magnetite, $Fe^{3+}[Fe^{3+}Fe^{2+}]O_4$ in which an ordering of Fe^{3+} and Fe^{2+} ions within octahedral sites is thought to occur below 125 K.

4.2 Investigation of polycrystalline $Fe_{3-x}Zn_xO_4$

4.2.1 X-ray diffractions and lattice parameters

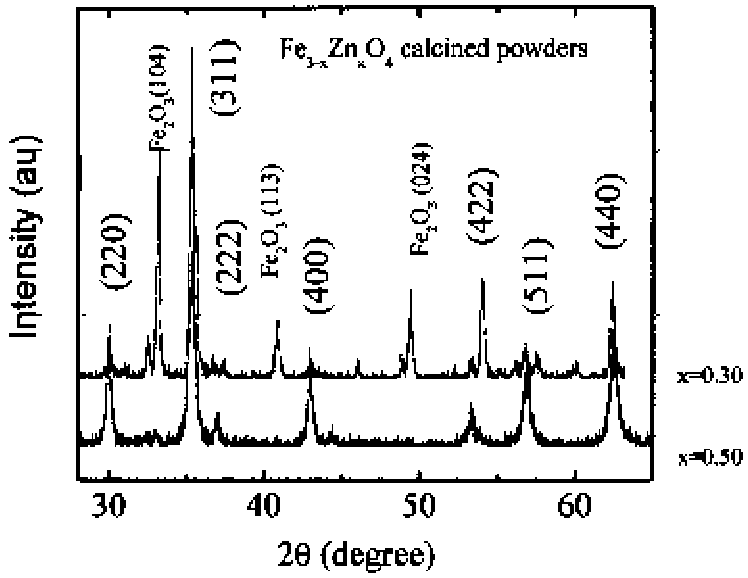

Figure 4. 22. The x-ray diffraction pattern of calcined $Fe_{3-x}Zn_xO_4$ ($x = 0.30$ and 0.50) powders.

The x-ray diffraction (XRD) patterns for the calcined samples $Fe_{3-x}Zn_xO_4$ ($x = 0.30$ and 0.5) and samples sintered at 750°C are presented in Figs. 4.22 and 4.23, respectively. Their diffraction peak positions with Miller indices are presented in Table 4.4. The XRD patterns for these sintered samples confirm the formation of spinel ferrite with a few unidentified peaks [1]. The values of lattice parameter '*a*' from all the peaks for the samples are plotted against Nelson-Riley function, *F(θ)* as shown in Fig. 4.24.

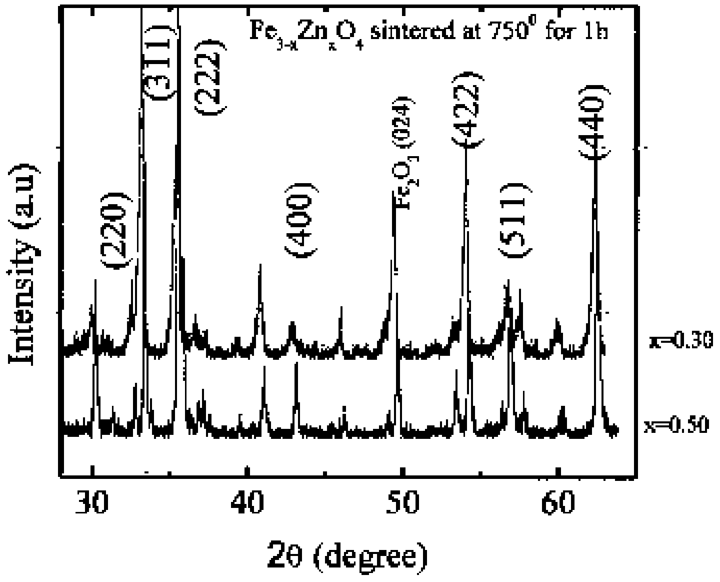

Figure 4.23. The X-ray diffraction pattern of polycrystalline $Fe_{3-x}Zn_xO_4$ sintered at 750°C for 1h.

The values of lattice parameter '*a*' from all the spinel peaks are plotted against Nelson-Riley function, *F(θ)*, for the sample sintered at 750°C is shown in Figs. 4.24, and 2.25. The calculated *a* and a_0 are presented in Table 4.5.

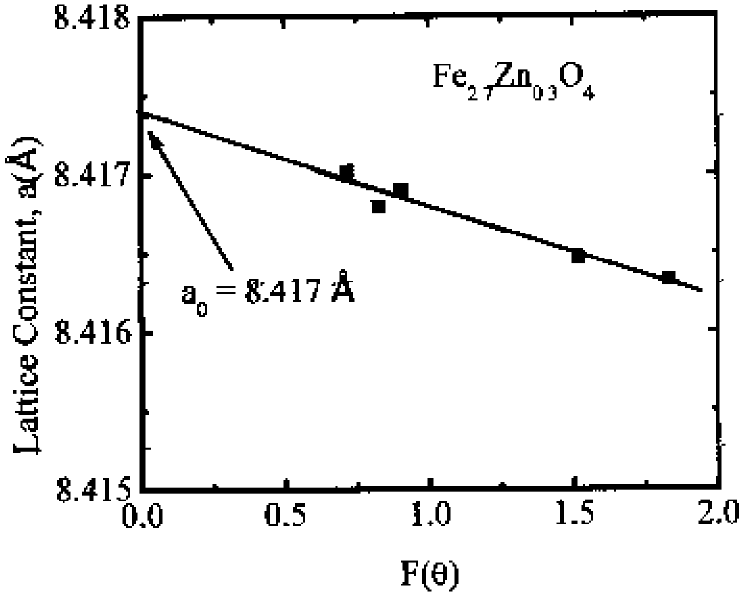

Figure 4.24. The variation of lattice constant 'a' with F(θ) for the $Fe_{2.7}Zn_{0.3}O_4$.

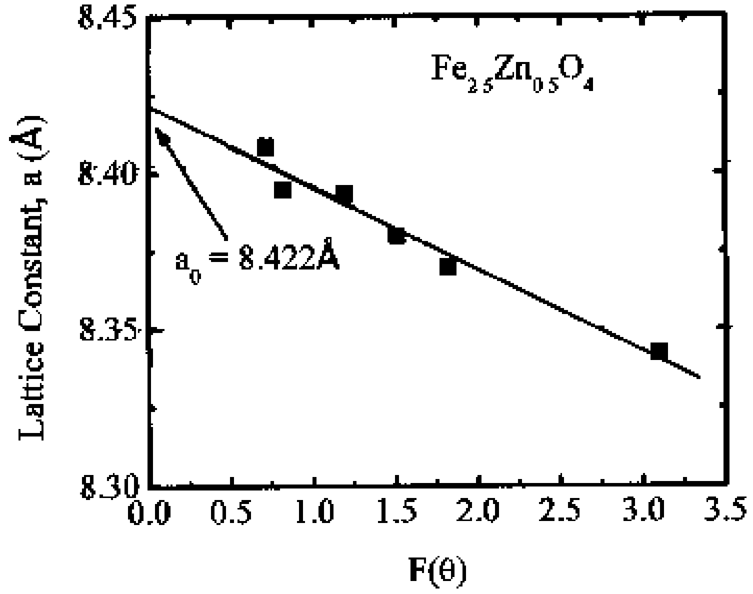

Figure 4.25. The variation of lattice constant 'a' with F(θ) for $Fe_{2.5}Zn_{0.5}O_4$.

107492

Table 4.4 X-ray peak positions for polycrystalline $Fe_{3-x}Zn_xO_4$ sintered at 750°C for 1h.

Sample composition	X-ray peak position with Miller indices 2θ (degree)				
	(111)	*(311)*	*(422)*	*(511)*	*(440)*
$Fe_{3-x}Zn_xO_4$(x =0.30)	19.98	35.59	54.00	56.81	62.33
$Fe_{3-x}Zn_xO_4$(x= 0.50)	18.42	35.53	54.55	57.01	62.48

From the figure we see that the lattice constant or $Fe_{2.5}Zn_{0.5}O_4$ (x = 0.50) and $Fe_{2.7}Zn_{0.3}O_4$ (x = 0.30) are 8.422 Å and 8.418 Å respectively. The lattice constant decreases as we decrease the Zn concentration. In comparison with the beach sand we see that the lattice constant for beach sand is smaller than $Fe_{2.5}Zn_{0.5}O_4$ (x = 0.50) and greater than $Fe_{2.7}Zn_{0.3}O_4$ (x = 0.30).

The increase in lattice parameter with increasing *Zn* content can be explained on the basis of the ionic radii. The ionic radii of the cations used in $Fe_{3-x}Zn_xO_4$ are 0.88Å (Zn^{2+}) and 0.69Å (Fe^{3+}) [2,3,6]. Since the ionic radius of Fe^{3+} is less than that of the Zn^{2+}, decrease in lattice constant with the decrease in *Zn* substitution is expected.

Table 4.5 The lattice parameters and true lattice parameters for $Fe_{3-x}Zn_xO_4$ sintered at 750°C for 1 h.

Sample	*peaks*	*Sintering Temp: T_s(°C)*	*(Å)*	
			a	(a_0)
$Fe_{2.7}Zn_{0.3}O_4$	1	750°	8.4160	8.418
	2		8.4165	
	3		8.4167	
	4		8.4169	
	5		8.4170	
$Fe_{2.5}Zn_{0.5}O_4$	1		8.3424	8.422
	2		8.3700	
	3		8.3930	
	4		8.3940	
	5		8.4080	

4.2.2 DC magnetization of polycrystalline $Fe_{3-x}Zn_xO_4$

The temperature dependent magnetization, M(T), for $Fe_{2.5}Zn_{0.5}O_4$ is measured in presence of 50 mT applied field in both ZFC and FC modes as shown in Fig. 4.26.

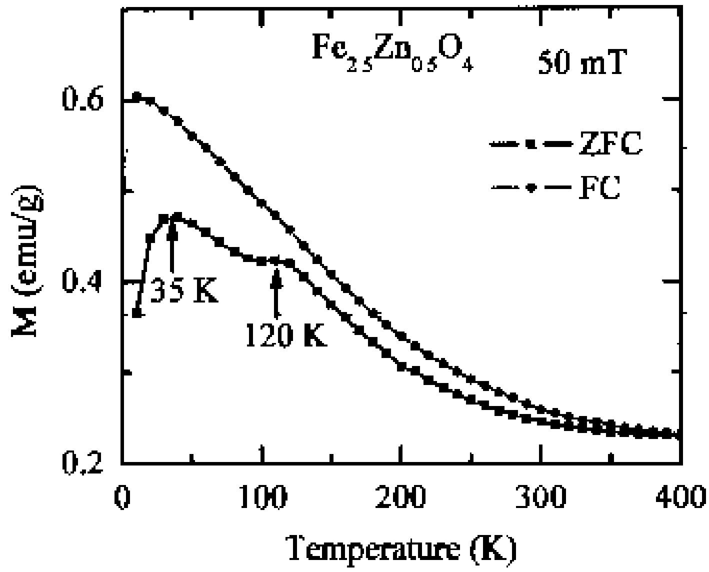

Figure 4.26 The temperature dependent magnetization for $Fe_{2.5}Zn_{0.5}O_4$ measured in presence of 50 mT applied field in FC and ZFC mode.

It was observed that in ZFC mode sample shows two transitions, one at 120K, perhaps corresponding to Verwey transition and another transition like features at 35 K.

The magnetization as a function of applied magnetic field, *M(H)*, for $Fe_{2.5}Zn_{0.5}O_4$ is measured both at room temperature (300K) and at 10K as shown in Fig. 4.27. The magnetization of $Fe_{2.5}Zn_{0.5}O_4$ increases almost linearly with increasing the applied magnetic field up to 1 T with two different slopes. No saturation is occurred in case of both temperatures. However, there is a hysteresis like features is observed, which is higher at 10 K. Such a conclusion is in agreement with that previously reported in case of *Zn-Co* ferrites [15,16].

In both M(T) and M(H) plots, it is observed that there is a drastic decrease of magnetization value due to substitution of nonmagnetic Zn in Fe_3O_4.

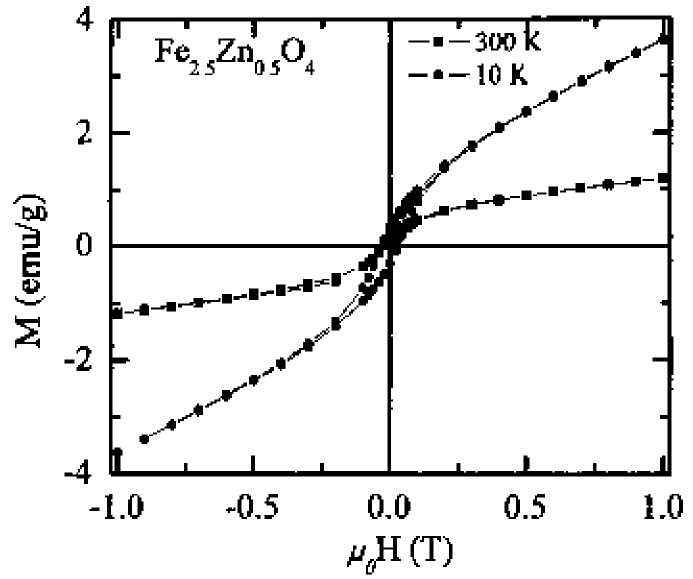

Figure 4.27 The magnetization as a function of applied magnetic field plots for $Fe_{2.5}Zn_{0.5}O_4$ measured at 10K and 300 K.

The temperature dependent magnetization, M(T), for $Fe_{2.7}Zn_{0.3}O_4$ is measured in presence of 50 mT applied field in both ZFC and FC modes as shown in Fig. 4.28. It is observed that in ZFC mode sample shows two transitions, one at 125, perhaps corresponding to Verwey transition and another at 35 K.

The magnetization as a function of applied magnetic field, *M(H)*, for $Fe_{2.7}Zn_{0.3}O_4$ measured both at room temperature (300K) and at 10K as shown in Fig. 4.29 The magnetization of $Fe_{2.7}Zn_{0.3}O_4$ increases almost linearly with increasing the applied magnetic field up to 1 T with two different slopes. The magnetization value is less than that of $Fe_{2.5}Zn_{0.5}O_4$. No saturation is occurred in case of both temperatures. However, there is a hysteresis like features is observed, which is higher at 10 K.

Like $Fe_{2.5}Zn_{0.5}O_4$, in both M(T) amd M(H) plots, it is observed that there is a drastic decrease of magnetization value due to substitution of nonmagnetic Zn in Fe_3O_4.

It is observed that the sample which contains higher concentration of *Zn* has lower magnetization value. This is due to the fact that inclusion of nonmagnetic *Zn* weakens the *A-B* magnetic interaction among the cations and hence lower magnetization. [17].

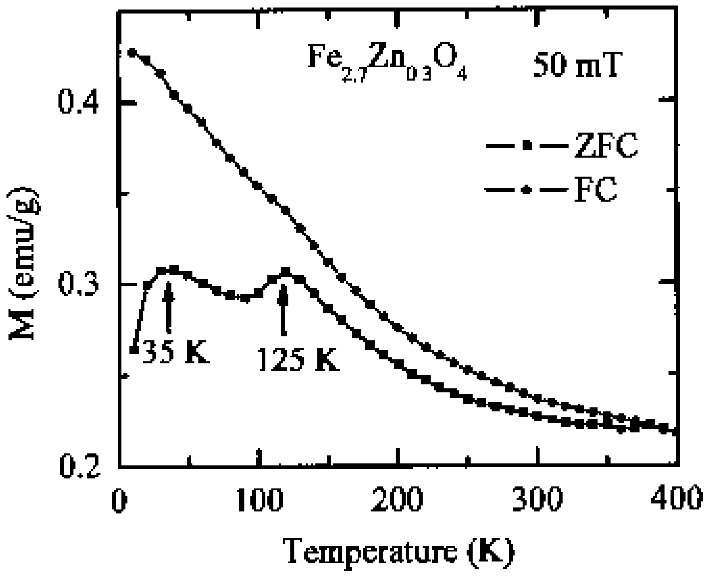

Figure 4.28 The temperature dependent magnetization for $Fe_{2.7}Zn_{0.3}O_4$ measured in presence of 50 mT applied field in FC and ZFC mode.

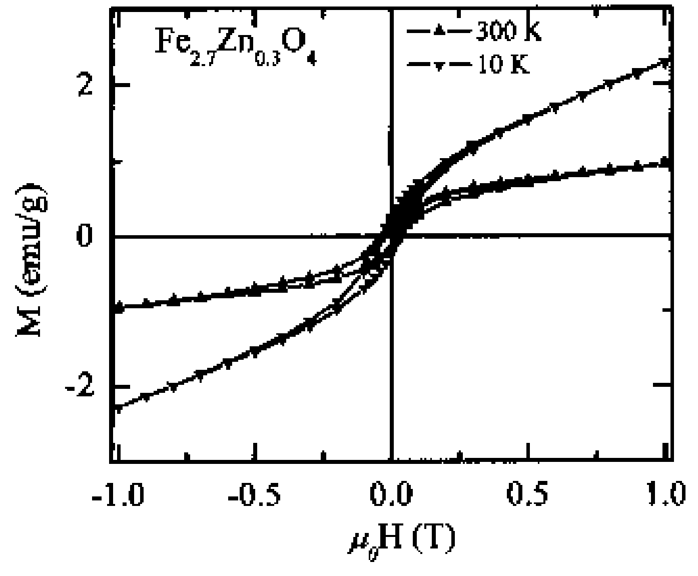

Figure 4.29 The magnetization as a function of applied magnetic field plots for $Fe_{2.7}Zn_{0.3}O_4$ measured at 10K and 300 K.

4.2.3 Complex permeability of polycrystalline $Fe_{3-x}Zn_xO_4$

Figs. 4.30 and 4.31 show the real and imaginary permeability spectra for $Fe_{3-x}Zn_xO_4$ (x = 0.30, 0.50) samples respectively. It is observed that the permeability value increases with increasing *Zn* content. Similar result is obtained by other authors in Ni-Zn ferrites [18].

. In $Fe_{2.5}Zn_{0.5}O_4$ (x = 0.50) samples, the maximum value of μ_i' is approximately 29.

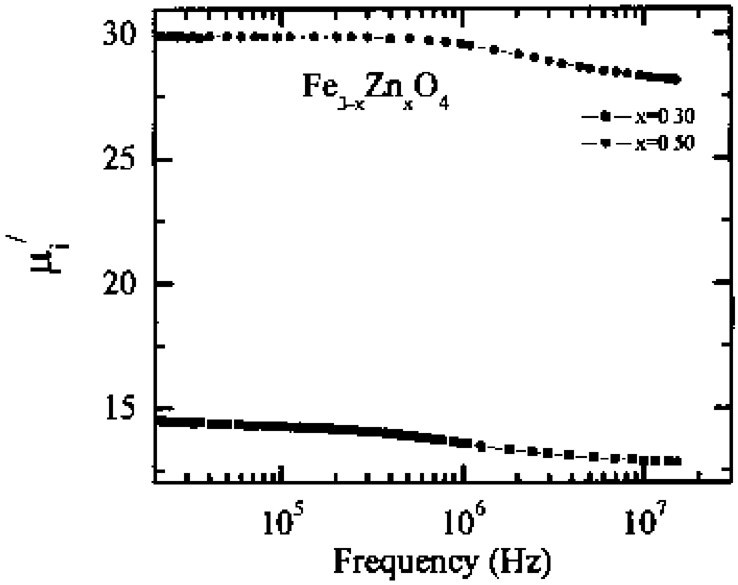

Figure 4.30. The μ_i' spectra for $Fe_{3-x}Zn_xO_4$ sintered at 750°C for 1hr in air.

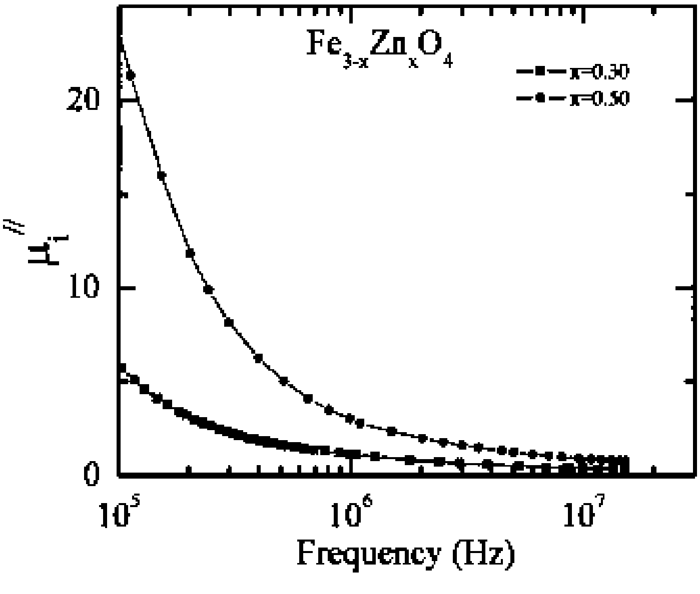

Figure 4.31. The μ_i'' spectra for for $Fe_{3-x}Zn_xO_4$ sintered at750°C for 1hr in air.

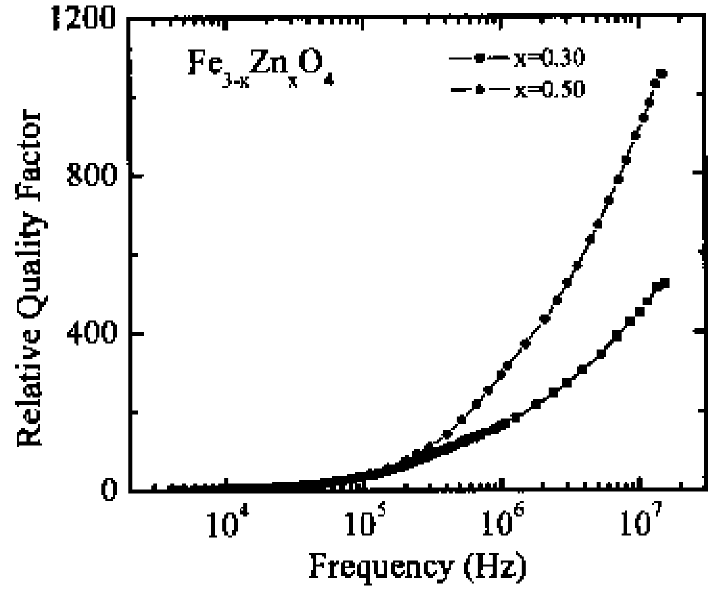

Figure 4.32. The variation of relative quality factor with frequency for polycrystalline $Fe_{3-x}Zn_xO_4$ samples sintered at 750°C for 1 hr.

Fig. 4.32 shows the variations of relative quality factor (or *Q* factor) as a function of frequency for $Fe_{3-x}Zn_xO_4$ sintered at 750°C for 1hr in air. From this figure, it is observed that *Q* factor increases due to Zn substitution in Fe_3O_4. For inductors used in filter applications, the quality factor is often used as a measure of performance. [19]

References

[1] A. K. M. Akther Hossain, M. Seki, T. Kawai and H. Tabata, "Colossal magnetoresistance in spinel type $Zn_{1-x}Ni_xFe_2O_4$," *J. Appl. Phys.*, **96**, 1273 (2004).

[2] J. E. Huhecy, E. A. Keiter, R. L. Keiter. "Inorganic Chemistry Principles of Structure and Reactivity". *4th Edition*

[3] A. K. M. Akther Hossain, K. Khirul Kabir, M. Seki, T. Kawai, H. T abata, "Structural, AC, and DC magnetic properties of $Zn_{1-x}Co_xFe_2O_4$" *Journal of Physics and Chemistry of Solids* **68** 1933 –1939 (2007).

[4] S.T.Mahmud, A.K.M.Akther Hossain, A.K.M.Abdul Hakim, M.Seki, T.Kawai, H.Tabata, "Influence of microstructure on the complex permeability of spinel type Ni –Zn ferrite" *Journal of Magnetism and Magnetic Materials* **305** 269 –274 (2006).

[5] A. A. Sattar, H. M. El-Sayed, K. M. El-Shokrofy and M. M. El-Tabey, "Improvement of the magnetic properties of Mn-Ni-Zn ferrite by the non-magnetic Al^{3+} ion substitution," *J. Appl. Sci.*, **5**(1), 162 (2005).

[6] Verwey, E. J. W., Haayman, P. W. "Substance: Fe_3O_4 property: crystal structure, lattice parameters, low temperature phase" *Physica* **8**, 979(1941)

[7] FriedrichWalz "The Verwey transition—a topical review" *J. Phys.: Condens Matter* **14** (2002)

[8] Z. Tarnawski, A. Wiechec, M. Madej, D. Nowak, D. Owoc, G. Krol, Z. Kakol, L. Kolwicz-Chodak,
A. KozÅlowski and T. Dawid, "Studies of the Verwey Transition in Magnetite" *Proceedings of the School Superconductivity and Other Phenomena in Perovskites*, Warsaw 2004.

[9] B. D. Cullity, *Introduction to Magnetic Materials*, Addison-Wisley Publishing Company, Inc., California (1972).

[10] E. Cedillo, J. Ocampo, V. Rivera and R. Valenzuela, "An apparatus for the measurement of initial magnetic permeability as a function of temperature," *Journal of Physics F: Scientific Instrument*, 13, 383 (1980).

[11] R. Valenzuela, *Magnetic Ceramics*, Cambridge University Press, Cambridge (1994).

[12] F. Brailsford, *Physical Principles of Magnetism*, D. Van Nostrand Company Ltd., London (1966).

[13] J. L. Snoek, "Dispersion and absorptions in magnetic ferrites at frequencies above Mc/s," *hysica*, 14, 207 (1948).

[14] F. Brailsford, *Physical Principles of Magnetism*, D. Van Nostrand Company Ltd., London (1966).

[15] M. A. Ahmed and M. A. El Hiti, "Electrical and Dielectric properties of $Zn_{0.8}Co_{0.2}Fe_2O_4$," *J. Phys.*, III France 5, 775 (1995).

[16] S. R. Murthy, "Low temperature sintering of MgCuZn ferrite and its electrical and magnetic properties," *Bull. Mater. Sci.*, 24(4), 379 (2001).

[17] Y. Yafet and C.Kittel, , " Antiferromagnetic arrangements in ferrites" *Physical . Review.* 87, 290 (1952).

[18] A.K.M.Akther Hossain, S.T.Mahmud, M.Seki, T.Kawai, H.Tabata, "Structural, electrical transport, and magnetic properties of $Ni_{1-x}Zn_xFe_2O_4$" *Journal of Magnetism and Magnetic Materials*.

[19] C. Wang, L. L. Zhou, X. Qi, Z. Yue, X. Wang, "Microstructures and high-frequency magnetic properties of low-temperature sintered Co –Ti substituted barium ferrites" *Journal of Magnetism and Magnetic Materials*, 257, 100-106 (2003).

CHAPTER 5

CONCLUSIONS

The Fe_3O_4 separated from the beach sand successfully. The XRD patterns of raw and sintered Fe_3O_4 clearly indicate formation of spinel structure with some other reflections from associated impurities. Some of the impurity peaks are perhaps due to the presence of hematite (Fe_2O_3). Besides these, some other unidentified peaks are also present in the XRD pattern. This suggests that our magnetic separation process is not sufficient to get phase pure magnetite from the Cox's Bazar beach sand. From the XRD pattern it is concluded that the Fe_3O_4 sintered at 750°C is more pure compared to raw and other sintered Fe_3O_4.

The lattice constant of Fe_3O_4.is found to be 8.403Å for the Fe_3O_4 sintered at 750°C. This value agrees well with the value for phase pure Fe_3O_4 observed by other authors. It is observed that the bulk density varies both as a function of sintering temperatures and times. The highest density 4.7 g/cm^3 is also fairly close (within 10%) the single crystal density 5.2 g/cm^3.

The M(T) plots of both raw and sintered Fe_3O_4 exhibit Verwey transition at 125 K, which is a characteristic features of Fe_3O_4. The M-H plots for these sample proved that these are soft magnetic materials. The M value increases linearly with increasing the applied magnetic field up to 0.2 T at both the room temperature (300K) and 10K temperatures and attains its saturation value for fields higher than 0.2 T. The 98% of saturation is observed at 0.3 T applied magnetic filed. The saturation magnetization at 10 K for raw Fe_3O_4 is 62.5 emu/g.. This saturation magnetization is corresponds to 2.61 μ_B. The saturation magnetization at 10 K for Fe_3O_4 sintered at 750°C for 1h is 83.5 emu/g. This saturation magnetization is corresponds to 3.5 μ_B.

It was found that due to sintering saturation magnetization value increases significantly as a result of sintering., However, present value is less than that of the saturation magnetization value (4 μ_B) of single crystal Fe_3O_4. For this sample the saturation magnetization value is about 88 % of the phase pure Fe_3O_4.

The μ_r' and μ_r'' values for Fe_3O_4 samples show a slightly variation with on sintering time and temperature. The μ_i' is highest for the sample sintered at 1000°C for 0.2h. Only the sample sintered at 950°C show the resonance frequency in the measured frequency range. For other sample, resonance frequency is beyond 13 MHz. At fixed dwell sintering time 1 hr, these samples also show a slight variation of μ_i' depending on sintering temperature. In this fixed sintering time μ_r', is the highest at 750°C. In both variations there is no peak or increasing tendency of μ_r'' with frequency, so it is also conclude that the resonance frequency is beyond the measured frequency range. It is also observed that for a fixed sintering temperature 900°C, μ_r' values increases and μ_r'' decreases with increasing furnaces soak time.

From the loss factor we have calculated the relative quality factor (or *Q* factor) for Fe_3O_4, The *Q* factor varies with sintering time temperature. It is observed that the Fe_3O_4 sintered at 750°C for 1 h has the highest *Q* value.

Resistance of magnetite sample sintered at 750°C for 1 h is measured at zero field and in the presence of 9 T magnetic field. Both measurements show an electron ordering transition in the R-T plots at about 125 K. This is known as famous Verwey transition. Similar type of transition is also observed in M(T) measurement at the same temperature for Fe_3O_4.

The XRD patterns of all compositions $Fe_{3-x}Zn_xO_4$ (x = 0.30 and 0.5) clearly indicate formation of spinel structure along with impurity peaks. The lattice constants are 8.418Å and 8.422Å for compositions $Fe_{2.7}Zn_{0.3}O_4$ and $Fe_{2.5}Zn_{0.5}O_4$, respectively. In comparison with the Fe_3O_4 (collected from beach sand) we observed that the lattice constant of $Fe_{3-x}Zn_xO_4$ (x = 0.30 and 0.5) is greater than Fe_3O_4. This can be explaining on the basis of the ionic radii. The radius of the Zn^{2+} (0.82 Å) is greater than that of the Fe^{3+}(0.69 Å) So greater lattice constant with *Zn* substitution is expected.

The magnetization as a function of applied magnetic field, for $Fe_{3-x}Zn_xO_4$ (x = 0.30 and 0.5) in both at 300K and at 10K. The magnetization of both samples increases almost linearly with increasing the applied magnetic field up to 1 T with different slopes, and No saturation is occurred in these temperature. However, a hysterisis like features is observed. Which is higher at 10 K. In both M(T) and M(H) plots, it is observed that there is a drastic decrease of magnetization value due to substitution of nonmagnetic Zn in Fe_3O_4. This is due to the fact that inclusion of nonmagnetic *Zn* weakens the *A-B* magnetic interaction among the cations and hence lower magnetization.

The μ_i' and Q factor increases with increasing *Zn* content in $Fe_{3-x}Zn_xO_4$. It is believed that due to substitution Zn the microstructure of the sample has improved which in turn increase the initial permeability and also quality factor. For inductors used in filter applications, the quality factor is often used as a measure of performance.

……………………